Astronomy: Faculty Publications

Astronomy

2-27-2015

Probing Stellar Accretion with Mid-Infrared Hydrogen Lines

Elisabetta Rigliaco
University of Arizona

Ilaria Pascucci
University of Arizona

Gaspard Duchene
University of California - Berkeley

Suzan Edwards
Smith College, sedwards@smith.edu

D. R. Ardila
California Institute of Technology

See next page for additional authors

Recommended Citation

Authors

Elisabetta Rigliaco, Ilaria Pascucci, Gaspard Duchene, Suzan Edwards, D. R. Ardila, C. Grady, Ignacio Mendigutía, Benjamín Montesinos, Gijs D. Mulders, Joan R. Najita, J. Carpenter, Elise Furlan, Uma Gorti, Rowin Meijerink, and M. R. Meyer

PROBING STELLAR ACCRETION WITH MID-INFRARED HYDROGEN LINES

Elisabetta Rigliaco[1,2], I. Pascucci[1], G. Duchene[3,4,5], S. Edwards[6], D. R. Ardila[7,8], C. Grady[9,10],
I. Mendigutía[11], B. Montesinos[12], G. D. Mulders[1], J. R. Najita[13], J. Carpenter[14],
E. Furlan[15], U. Gorti[16,17], R. Meijerink[18], and M. R. Meyer[2]

[1] Department of Planetary Science, University of Arizona, 1629 E. University Blvd., Tucson, AZ 85719, USA;
rigliaco@lpl.arizona.edu, elisabetta.rigliaco@phys.ethz.ch
[2] Institute for Astronomy, ETH Zurich, Wolfgang-Pauli-Strasse 27, CH-8093 Zurich, Switzerland
[3] Astronomy Department, University of California, Berkeley, Hearst Field Annex B-20, Berkeley, CA 94720-3411, USA
[4] Universite de Grenoble Alpes, IPAG, F-38000 Grenoble, France
[5] CNRS, IPAG, F-38000 Grenoble, France
[6] Five College Astronomy Department, Smith College, Northampton, MA 01063, USA
[7] NASA Herschel Science Center, California Institute of Technology, MC 100-22, Pasadena, CA 91125, USA
[8] The Aerospace Corporation, M2-266, El Segundo, CA 90245, USA
[9] Eureka Scientific, 2452 Delmer Street, Suite 100, Oakland, CA 94602-3017, USA
[10] Exoplanets and Stellar Astrophysics Lab, Code 667, GoddardSpace Flight Center, Greenbelt, MD 20771, USA
[11] School of Physics and Astronomy, University of Leeds, Woodhouse Lane, Leeds LS2 9JT, UK
[12] Departamento de Astrofísica, Centro de Astrobiología, ESAC Campus, P.O. Box 78, E-28691 Villanueva de la Cañada, Madrid, Spain
[13] National Optical Astronomy Observatory, 950 North Cherry Avenue, Tucson, AZ 85719, USA
[14] Department of Astronomy, California Institute of Technology, MC 249-17, Pasadena, CA 91125, USA
[15] Infrared Processing and Analysis Center, California Institute of Technology, 770 S. Wilson Ave., Pasadena, CA 91125, USA
[16] NASA Ames Research Center, Moffett Field, CA 94035, USA
[17] SETI Institute, Mountain View, CA 94043, USA
[18] Leiden Observatory, Leiden University, P.O. Box 9513, NL-2300 RA Leiden, The Netherlands

ABSTRACT

In this paper we investigate the origin of the mid-infrared (IR) hydrogen recombination lines for a sample of 114 disks in different evolutionary stages (full, transitional, and debris disks) collected from the *Spitzer* archive. We focus on the two brighter H I lines observed in the *Spitzer* spectra, the H I (7–6) at 12.37 μm and the H I (9–7) at 11.32 μm. We detect the H I (7–6) line in 46 objects, and the H I (9–7) in 11. We compare these lines with the other most common gas line detected in *Spitzer* spectra, the [Ne II] at 12.81 μm. We argue that it is unlikely that the H I emission originates from the photoevaporating upper surface layers of the disk, as has been found for the [Ne II] lines toward low-accreting stars. Using the H I (9–7)/H I (7–6) line ratios we find these gas lines are likely probing gas with hydrogen column densities of 10^{10}–10^{11} cm^{-3}. The subsample of objects surrounded by full and transitional disks show a positive correlation between the accretion luminosity and the H I line luminosity. These two results suggest that the observed mid-IR H I lines trace gas accreting onto the star in the same way as other hydrogen recombination lines at shorter wavelengths. A pure chromospheric origin of these lines can be excluded for the vast majority of full and transitional disks. We report for the first time the detection of the H I (7–6) line in eight young (<20 Myr) debris disks. A pure chromospheric origin cannot be ruled out in these objects. If the H I (7–6) line traces accretion in these older systems, as in the case of full and transitional disks, the strength of the emission implies accretion rates lower than 10^{-10} $M_\odot$ yr^{-1}. We discuss some advantages of extending accretion indicators to longer wavelengths, and the next steps required pinning down the origin of mid-IR hydrogen lines.

Key words: accretion, accretion disks – circumstellar matter – infrared: stars – line: identification – stars: activity

1. INTRODUCTION

The analysis and characterization of circumstellar disks, which provide the raw material to form planets, are crucial for our understanding of disk dispersal and planet formation processes. Observations and modeling of the dust content in protoplanetary disks are nowadays relatively abundant (see Testi et al. 2014 for a review). The gaseous component of circumstellar disks is instead less well characterized (e.g., Dutrey et al. 2014 for a review) even if major advances have been made in the past few years thanks to space observatories such as *Spitzer* (e.g., Pontoppidan et al. 2014) and *Herschel* (e.g., Dent et al. 2013). Gas plays a pivotal role in the structure and evolution of disks representing the bulk of the disk mass (e.g., Alexander et al. 2014). It is then necessary to extend our knowledge of the disk gas content in order to improve our understanding of the natal environments of planets.

The sensitivity of the InfraRed Spectrograph (IRS) on the *Spitzer Space Telescope* led to the discovery of gas lines that can be used to characterize the immediate surroundings of young stellar objects (YSOs). For instance, the rich water spectrum of YSOs has been attributed to emission arising from warm (∼600 K) layers of water vapor out to a few AUs from the central star (Carr & Najita 2008, 2011; Salyk et al. 2008; Pontoppidan et al. 2010; Salyk et al. 2011; Banzatti et al. 2013).

Among the wide forest of lines revealed by *Spitzer* the most common one is the singly ionized neon, [Ne II] at 12.81 μm (e.g., Pascucci et al. 2007; Lahuis et al 2007; Güdel et al. 2010). Different studies of this line show that objects with known jets/outflows have higher [Ne II] luminosity than objects without (Güdel et al. 2010; Baldovin-Saavedra et al. 2011). Moreover, follow up observations of this line with ground-based high-resolution spectrographs have shown that [Ne II] is predominantly tracing an outflow in high-accreting stars, while

its origin is from photoevaporative disk winds driven by high-energy photons from the central star in lower accretors (Pascucci & Sterzik 2009; van Boekel et al. 2009; Sacco et al. 2012; Baldovin-Saavedra et al. 2012).

Other gas lines that are commonly used to characterize objects undergoing accretion are hydrogen recombination lines. H I lines from the near-ultraviolet (UV) to the near-infrared (near-IR) have been extensively used as indicators of the rate at which the matter from the inner circumstellar disk is accreting onto the star (e.g., Muzerolle et al. 2001; Calvet et al. 2004; Natta et al. 2006; Alcalà et al. 2014; Edwards et al. 2013; among many others). Recently, Salyk et al. (2013) using NIRSPEC at the Keck II telescope and CRIRES at the Very Large Telescope have introduced the H I Pfβ line at 4.65 μm as an accretion diagnostic. This is to date the longest wavelength hydrogen line proposed as an accretion indicator.

As early as 2007, Pascucci et al. (2007) have reported also the detection of H I lines in the *Spitzer* spectrum of RX1852.3-3700. Subsequently, Ratzka et al. (2007) and Najita et al. (2010) reported hydrogen line detections in both the low- and high-resolution *Spitzer* spectrum of TWHya. The analysis of these two objects did not constrain the origin of these lines and left several possibilities open: stellar chromosphere, hot disk atmosphere, accretion shock regions, or internal wind shock very close to the stellar surface (Hollenbach & Gorti 2009). More recently, Carr & Najita (2011) reported the detection of the IR hydrogen lines in 10 T Tauri stars but did not discuss their origin.

Here, we improve upon studies of gas lines from circumstellar disks by analyzing hydrogen lines observed in the *Spitzer*/IRS spectra of a large sample of objects. In particular we focus on the strongest of the Humphreys Series lines in the mid-IR, the Huα at 12.37 μm (hereafter H I (7–6)) and the H I (9–7) line at 11.31 μm. With the aim to investigate the origin of these mid-IR hydrogen lines, we compare their properties both with hydrogen lines observed at shorter wavelengths, mainly tracing accretion, and with the other most common gas line observed in the *Spitzer* spectra ([Ne II]) which is instead an outflow or disk wind tracer depending on the mass accretion rate.

The paper is organized as follows. In Section 2 the source selection and data reduction are explained. In Section 3 we describe the method used to account for the water contamination of the H I lines, and how we measure the H I and [Ne II] line fluxes and luminosities. In Section 4 we discuss the origin of the H I mid-IR lines, highlighting the interesting presence of H I lines in a sample of debris disks. The summary of the results and an outlook are given in Section 5.

2. SAMPLE SELECTION AND DATA REDUCTION

Using the *Spitzer* Heritage Archive[19] we downloaded and re-reduced all IRS Short-High (SH) spectra of disks-bearing young stars acquired in the Standard Staring Mode and which have multiple on-source exposures (*N*-cycle > 1) and sky observations. The latter two restrictions were applied to better identify and correct for bad pixels as summarized below. A list of the 114 objects identified in this way and with a signal-to-noise (S/N) on the continuum greater than 5 is reported in Table 1. This table also contains the source coordinates, the Astronomical Observation Request (AOR) number, the Identification Number (ID) of the *Spitzer* program the object belongs to, and the exposure time per frame times the number
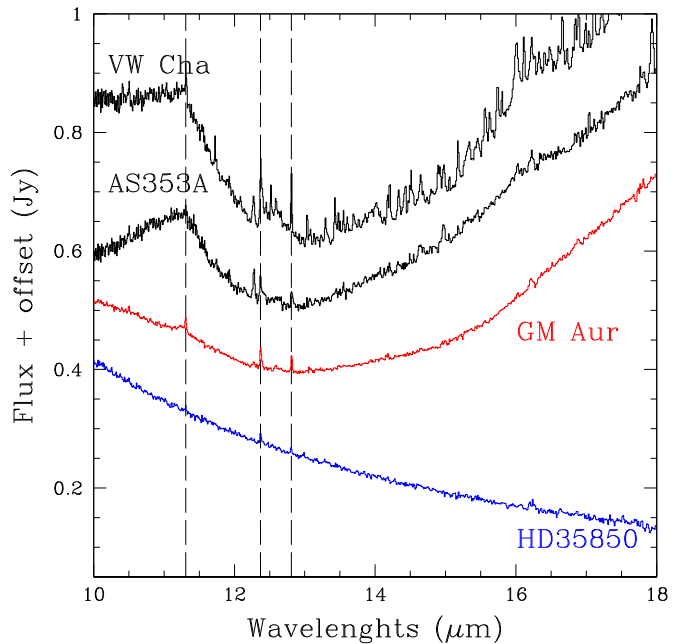
Figure 1. *Spitzer*/IRS SH spectra of four disks. For plotting purposes offsets have been applied as follows: −0.1 Jy at VWCha (water-contaminated full disk), −0.6 Jy at AS 353A (water-free full disk), +0.3 Jy at GM Aur (transitional disk), and 0.0 Jy at HD 35850 (debris disk). The vertical dashed lines show the location of the three lines mainly used through this paper: H I (7–6) at 12.37 μm, H I (9–7) at 11.32 μm, and [Ne II] at 12.81 μm.

of exposures. We also report in Table 5 the sources' properties, and in Table 6 the mid-IR line fluxes, errors, and continuum levels around the three line of interest.

The IRS SH module uses a cross-dispersed echelle design and covers the spectral range 9.9–19.6 μm with a nominal resolving power of $R \sim 600$ (Houck et al. 2004). The data reduction was performed starting from the *droopres* products following the procedure outlined in Pascucci et al. (2013). In brief, we computed the average of the on-source and sky exposures per nod position and rejected bad pixels using the noise statistics from multiple cycles. We then created background subtracted images and corrected for the additional known bad pixels reported in the IRS Basic Calibrated Data (BCD) mask. The one-dimensional spectrum was extracted from the background-subtracted pixel-corrected images using the full aperture extraction routine in SMART (Higdon et al. 2004). We applied the same procedure to our sources and to the *Spitzer* flux calibrator ξ Dra. From the reduction of 10 different exposures of ξ Dra and the known stellar model atmosphere we created two one-dimensional spectral response functions (one at each nod position). Finally, we divided the source spectra by the spectral response function. A compilation of four *Spitzer*/IRS SH spectra analyzed in this paper is shown in Figure 1.

The calibrated spectra of 54 sources belonging to program IDs 40247, 20363, 148, and 41 can be downloaded from the IRSA Spitzer Science Center at http://irsa.ipac.caltech.edu/data/SPITZER/Disks_SH_spectra.

The total sample includes objects classified according to their general disk properties. We use the generic term Full Disks (F) for those disks with strong excess emission above photospheric levels at IR wavelengths, starting in the near-IR. Transitional Disks (T) are broadly defined as disks with reduced near- and mid-IR excess fluxes but excess emission comparable to full disks beyond $\sim$20 μm, indicative of a depleted inner region.

Table 1
All Objects Reduced: Observing Log

Name	R.A.	Decl.	AOR	Program ID	Time×Ncycles
HD 377	$0^h08^m25\overset{s}{.}76$	$+6^d37^m00\overset{s}{.}3$	13462272	148	120×3
HD 12039	$1^h57^m48\overset{s}{.}97$	$-21^d54^m05\overset{s}{.}2$	13461760	148	120×4
HD 17925	$2^h52^m32\overset{s}{.}13$	$-12^d46^m11\overset{s}{.}0$	9780480	148	30×5
HD 19668	$3^h09^m42\overset{s}{.}28$	$-9^d34^m46\overset{s}{.}4$	13462784	148	120×3
LkHa 326	$3^h30^m44\overset{s}{.}01$	$+30^d32^m47\overset{s}{.}0$	27063552	50641	30×12
IC348-67	$3^h43^m44\overset{s}{.}62$	$+32^d08^m17\overset{s}{.}9$	22850816	40247	30×100
IC348-31	$3^h44^m18\overset{s}{.}16$	$+32^d04^m57\overset{s}{.}0$	22849280	40247	30×16
IC348-72	$3^h44^m22\overset{s}{.}58$	$+32^d01^m53\overset{s}{.}7$	22851840	40247	30×100
IC348-68	$3^h44^m28\overset{s}{.}51$	$+31^d59^m54\overset{s}{.}1$	22851328	40247	30×100
IC348-55	$3^h44^m31\overset{s}{.}36$	$+32^d00^m14\overset{s}{.}7$	22850304	40247	30×80
IC348-2	$3^h44^m35\overset{s}{.}36$	$+32^d10^m04\overset{s}{.}6$	22847744	40247	30×4
IC348-6	$3^h44^m36\overset{s}{.}94$	$+32^d06^m45\overset{s}{.}4$	22848256	40247	30×16
IC348-37	$3^h44^m37\overset{s}{.}99$	$+32^d03^m29\overset{s}{.}8$	22849792	40247	30×30
IC348-133	$3^h44^m41\overset{s}{.}74$	$+32^d12^m02\overset{s}{.}4$	22852352	40247	30×100
IC348-21	$3^h44^m56\overset{s}{.}15$	$+32^d09^m15\overset{s}{.}5$	22848768	40247	30×30
LkHa 330	$3^h45^m48\overset{s}{.}28$	$+32^d24^m11\overset{s}{.}9$	27063040	50641	30×7
HD 25457	$4^h02^m36\overset{s}{.}74$	$-0^d16^m08\overset{s}{.}1$	9779712	148	6×4
FM Tau	$4^h14^m13\overset{s}{.}58$	$+28^d12^m49\overset{s}{.}3$	24403968	30300	120×2
FN Tau	$4^h14^m14\overset{s}{.}59$	$+28^d27^m58\overset{s}{.}0$	27062528	50641	30×6
CW Tau	$4^h14^m17\overset{s}{.}00$	$+28^d10^m57\overset{s}{.}8$	27062272	50641	30×6
FP Tau	$4^h14^m47\overset{s}{.}30$	$+26^d46^m26\overset{s}{.}4$	26321408	50498	30×8
CX Tau	$4^h14^m47\overset{s}{.}86$	$+26^d48^m11\overset{s}{.}0$	23551744	40338	30×21
CY Tau	$4^h17^m33\overset{s}{.}72$	$+28^d20^m46\overset{s}{.}8$	27061504	50641	30×14
DD Tau	$4^h18^m31\overset{s}{.}13$	$+28^d16^m28\overset{s}{.}9$	26320384	50498	30×2
BP Tau	$4^h19^m15\overset{s}{.}84$	$+29^d06^m27\overset{s}{.}0$	14548224	20363	30×12
DE Tau	$4^h21^m55\overset{s}{.}67$	$+27^d55^m06\overset{s}{.}2$	27060992	50641	30×10
FT Tau	$4^h23^m39\overset{s}{.}18$	$+24^d56^m14\overset{s}{.}3$	27060224	50641	30×14
04216+2603	$4^h24^m44\overset{s}{.}58$	$+26^d10^m14\overset{s}{.}2$	27059968	50641	30×12
IP Tau	$4^h24^m57\overset{s}{.}08$	$+27^d11^m56\overset{s}{.}3$	24404224	30300	120×5
DG Tau	$4^h27^m04\overset{s}{.}70$	$+26^d06^m15\overset{s}{.}8$	14547968	20363	6×12
DH Tau	$4^h29^m41\overset{s}{.}57$	$+26^d32^m58\overset{s}{.}2$	26320128	50498	30×10
UX TauA	$4^h30^m04\overset{s}{.}00$	$+18^d13^m49\overset{s}{.}4$	18013952	30300	30×30
DK Tau	$4^h30^m44\overset{s}{.}28$	$+26^d01^m24\overset{s}{.}6$	14548736	20363	30×8
HK Tau	$4^h31^m50\overset{s}{.}58$	$+24^d24^m17\overset{s}{.}8$	27059200	50641	30×14
FZ Tau	$4^h32^m31\overset{s}{.}77$	$+24^d20^m02\overset{s}{.}6$	27058688	50641	30×6
HN Tau	$4^h33^m39\overset{s}{.}36$	$+17^d51^m52\overset{s}{.}3$	27058176	50641	30×6
DL Tau	$4^h33^m39\overset{s}{.}08$	$+25^d20^m38\overset{s}{.}1$	27058432	50641	30×6
DM Tau	$4^h33^m48\overset{s}{.}72$	$+18^d10^m10\overset{s}{.}0$	18014720	30300	30×30
AA Tau	$4^h34^m55\overset{s}{.}44$	$+24^d28^m53\overset{s}{.}4$	14551552	20363	30×12
DN Tau	$4^h35^m27\overset{s}{.}37$	$+24^d14^m58\overset{s}{.}9$	24404480	30300	30×9
DO Tau	$4^h38^m28\overset{s}{.}58$	$+26^d10^m49\overset{s}{.}4$	14548480	20363	30×8
LkCa 15	$4^h39^m17\overset{s}{.}80$	$+22^d21^m03\overset{s}{.}5$	23551488	40338	30×21
04385+2550	$4^h41^m38\overset{s}{.}82$	$+25^d56^m27\overset{s}{.}0$	27057408	50641	30×6
DP Tau	$4^h42^m37\overset{s}{.}69$	$+25^d15^m37\overset{s}{.}3$	27057152	50641	30×6
DQ Tau	$4^h46^m53\overset{s}{.}06$	$+17^d00^m00\overset{s}{.}4$	26321152	50498	30×2
DR Tau	$4^h47^m06\overset{s}{.}22$	$+16^d58^m42\overset{s}{.}9$	27067136	50641	6×12
DS Tau	$4^h47^m48\overset{s}{.}60$	$+29^d25^m11\overset{s}{.}6$	26320896	50498	30×4
UY Aur	$4^h51^m47\overset{s}{.}38$	$+30^d47^m13\overset{s}{.}9$	14551040	20363	6×10
St 34	$4^h54^m23\overset{s}{.}68$	$+17^d09^m53\overset{s}{.}5$	18016256	30300	30×40
GM Aur	$4^h55^m10\overset{s}{.}98$	$+30^d21^m59\overset{s}{.}5$	18015488	30300	30×10
SU Aur	$4^h55^m59\overset{s}{.}38$	$+30^d34^m01\overset{s}{.}5$	27066880	50641	6×10
HD 32297	$5^h02^m27\overset{s}{.}44$	$+7^d27^m39\overset{s}{.}7$	25677568	50150	30×5
V836 Tau	$5^h03^m06\overset{s}{.}60$	$+25^d23^m19\overset{s}{.}7$	23552000	40338	30×21
RW Aur	$5^h07^m49\overset{s}{.}56$	$+30^d24^m05\overset{s}{.}0$	14547200	20363	6×13
HD 35850	$5^h27^m04\overset{s}{.}76$	$-11^d54^m03\overset{s}{.}5$	9777920	148	30×6
HD 37484	$5^h37^m39\overset{s}{.}62$	$-28^d37^m34\overset{s}{.}7$	9780224	148	30×10
NGC 2068/2071-H9	$5^h46^m11\overset{s}{.}86$	$+0^d32^m25\overset{s}{.}9$	22853888	40247	30×100
NGC 2068/2071-S1	$5^h46^m18\overset{s}{.}89$	$-0^d05^m38\overset{s}{.}2$	22854912	40247	30×50
NGC 2068/2071-H13	$5^h46^m22\overset{s}{.}44$	$-0^d08^m52\overset{s}{.}6$	22854400	40247	30×80
AO Men	$6^h18^m28\overset{s}{.}24$	$-72^d02^m41\overset{s}{.}7$	5458688	148	120×2
HD 61005	$7^h35^m47\overset{s}{.}47$	$-32^d12^m14\overset{s}{.}2$	13462528	148	120×3
HD 69830	$8^h18^m23\overset{s}{.}95$	$-12^d37^m55\overset{s}{.}8$	12710656	41	30×2
SX Cha	$10^h55^m59\overset{s}{.}76$	$-77^d24^m40\overset{s}{.}1$	27066624	50641	30×7
TW Cha	$10^h56^m30\overset{s}{.}52$	$-77^d11^m39\overset{s}{.}4$	27066368	50641	30×28
SZ Cha	$10^h58^m16\overset{s}{.}77$	$-77^d17^m17\overset{s}{.}1$	22846208	40247	30×4

Table 1
(Continued)

Name	R.A.	Decl.	AOR	Program ID	Time×Ncycles
TW Hya	$11^h01^m51^s91$	$-34^d42^m17^s0$	18017792	30300	30×2
CS Cha	$11^h02^m24^s91$	$-77^d33^m35^s7$	18021632	30300	30×50
Ced110-IRS2	$11^h06^m15^s41$	$-77^d21^m56^s8$	18022400	30300	30×10
Ced110-IRS4	$11^h06^m46^s58$	$-77^d22^m32^s6$	18019328	30300	30×36
Sz 18	$11^h07^m19^s15$	$-76^d03^m04^s8$	18020864	30300	30×100
VW Cha	$11^h08^m01^s47$	$-77^d42^m28^s7$	27066112	50641	30×6
Sz 27	$11^h08^m39^s05$	$-77^d16^m04^s2$	22847232	40247	30×100
VZ Cha	$11^h09^m23^s79$	$-76^d23^m20^s8$	27065856	50641	30×8
WX Cha	$11^h09^m58^s74$	$-77^d37^m09^s0$	27065600	50641	30×12
Hen 3-600A	$11^h10^m27^s53$	$-37^d31^m53^s6$	18018560	30300	30×2
XX Cha	$11^h11^m39^s66$	$-76^d20^m15^s3$	27065344	50641	30×14
RX J1111.7-7620	$11^h11^m46^s31$	$-76^d20^m09^s1$	5451776	148	30×6
CHX22	$11^h12^m42^s69$	$-77^d22^m23^s1$	22846720	40247	30×60
1RXS J121236.4-552037	$12^h12^m35^s77$	$-55^d20^m27^s4$	5460992	148	120×6
1RXS J122233.4-533347	$12^h22^m33^s23$	$-53^d33^m48^s9$	13463296	148	120×6
TWA 10	$12^h35^m04^s30$	$-41^d36^m39^s0$	22934528	40338	30×10
Sz 50	$13^h00^m55^s38$	$-77^d10^m22^s1$	27065088	50641	30×14
1RXS J130153.7-530446	$13^h01^m50^s69$	$-53^d04^m58^s1$	13462016	148	120×6
1RXS J132207.2-693812 (MPMus)	$13^h22^m07^s54$	$-69^d38^m12^s1$	5451264	148	6×3
1RXS J133758.0-413448	$13^h37^m57^s30$	$-41^d34^m42^s0$	5460224	148	120×6
HD 119269	$13^h43^m28^s54$	$-54^d36^m43^s5$	5461248	148	120×2
HD 134319	$15^h05^m49^s91$	$+64^d02^m50^s0$	9779968	148	30×6
V343Nor	$15^h38^m57^s56$	$-57^d42^m27^s3$	5458944	148	120×2
HT Lup	$15^h45^m12^s87$	$-34^d17^m30^s6$	27064832	50641	6×10
GQ Lup	$15^h49^m12^s11$	$-35^d39^m04^s8$	27064576	50641	30×8
HD 141943	$15^h53^m27^s30$	$-42^d16^m00^s8$	5462528	148	120×4
HD 142361	$15^h54^m59^s86$	$-23^d47^m18^s2$	5461504	148	120×12
IM Lup	$15^h56^m09^s21$	$-37^d56^m05^s9$	27064320	50641	30×6
RU Lup	$15^h56^m42^s31$	$-37^d49^m15^s5$	27064064	50641	30×5
HD 143006	$15^h58^m36^s93$	$-22^d57^m15^s4$	9777152	148	6×8
RX J1600.6-2159	$16^h00^m40^s57$	$-22^d00^m32^s3$	17145344	148	120×9
EX Lup	$16^h03^m05^s49$	$-40^d18^m25^s3$	27063808	50641	30×6
RX J1612.6-1859	$16^h12^m40^s51$	$-18^d59^m28^s3$	5457664	148	120×4
RXJS J161410.6-230542	$16^h14^m11^s08$	$-23^d05^m36^s2$	5453824	148	30×2
1RXS J161458.4-275013	$16^h14^m59^s17$	$-27^d50^m23^s0$	17144832	148	120×9
DoAr 21	$16^h26^m03^s03$	$-24^d23^m36^s4$	24403456	30300	30×6
DoAr 24E	$16^h26^m23^s42$	$-24^d21^m00^s5$	27062784	50641	30×5
DoAr 25	$16^h26^m23^s69$	$-24^d43^m14^s0$	24403712	30300	120×4
SR 21	$16^h27^m10^s20$	$-24^d19^m16^s0$	24403200	30300	6×10
Haro 1-16	$16^h31^m33^s46$	$-24^d27^m37^s4$	27062016	50641	30×7
RNO 90	$16^h34^m09^s17$	$-15^d48^m16^s8$	27061760	50641	6×9
WaOph6	$16^h48^m45^s63$	$-14^d16^m36^s0$	27060736	50641	30×6
EC 82	$18^h29^m56^s90$	$+1^d14^m46^s5$	27059712	50641	30×8
RX J1842.9-3532	$18^h42^m57^s97$	$-35^d32^m42^s7$	5451521	148	30×5
RX J1852.3-3700	$18^h52^m17^s30$	$-37^d00^m11^s9$	5452033	148	120×2
AS 353A	$19^h20^m30^s98$	$+11^d01^m54^s8$	14547456	20363	30×8
V1331 Cyg	$21^h01^m09^s20$	$+50^d21^m44^s5$	14547712	20363	30×8
HD 202917	$21^h20^m49^s96$	$-53^d02^m03^s2$	9778176	148	30×5
HD 216803	$22^h56^m24^s05$	$-31^d33^m56^s1$	9777664	148	30×5

Finally, Debris Disks (D) are defined in this paper as having pure photosphere emission out to about 10 μm but can have relatively small excess emission in the long portion of the mid-IR spectrum. This disk classification collected from the literature is based on the dust properties and the continuum spectral energy distributions, and it is mainly taken from Furlan et al. (2006, 2011), Espaillat et al. (2012), Silverstone et al. (2006), and Chen et al. (2014), as reported in Table 5. Most of the debris disks included in our study belong to the recent catalog published by Chen et al. (2014). Full and transitional disks are primordial, gas-rich disks, while debris disks are second-generation disks, dominated by dust. In total our sample includes 68 full, 21 transitional, and 25 debris disks. In Figure 2 we show the distribution in mass, luminosity, effective temperature, and accretion luminosity (see Section 3.2) for the total sample, and for the objects where the H I (7–6) line is detected. A K-S two-sample test of the stellar properties shows the two data sets have most likely the same parent distribution.

3. ANALYSIS AND IMMEDIATE RESULTS

In the following, we summarize the main properties of our sample (Section 3.1), compute accretion luminosities for each object in a self consistent manner (Section 3.2), and describe in
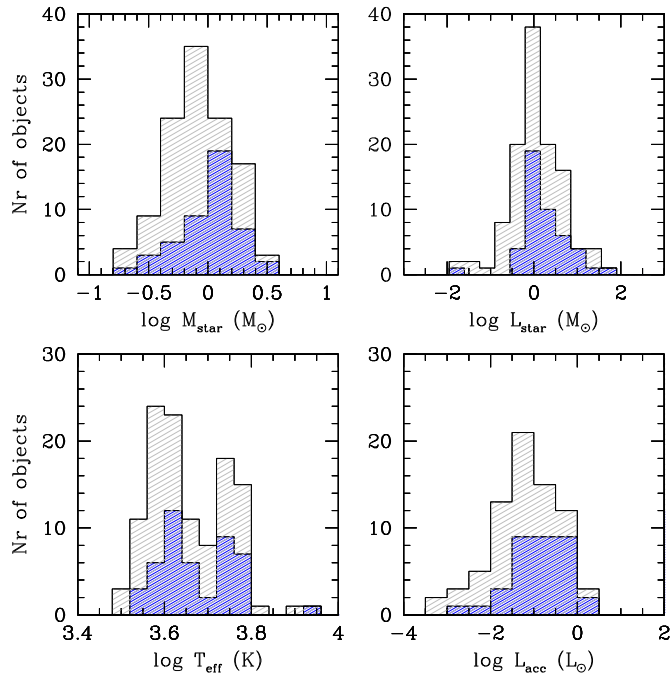
Figure 2. Distribution of mass, luminosity, effective temperature and accretion luminosity for all the objects in our sample (gray), and only the objects where H I (7–6) line has been detected (blue).

detail how we calculate [Ne II] and H I fluxes taking into account any possible contamination from water lines (Sections 3.3 and 3.4). The last two sections (Sections 3.5 and 3.6) discuss detections and correlations between line fluxes and adjacent continuum emission.

3.1. Subsample of H I and [Ne II] Sources: Star and Disk Properties

The properties of the 114 objects are summarized in Table 5. For each object we provide the stellar association it belongs to, the distance, spectral type (SpTy), visual extinction (A_V) as well as the effective temperature (T_{eff}) obtained using the T_{eff}–SpTy correlation of Kenyon & Hartmann (1995) and Luhman et al. (2003). Hα equivalent widths and stellar luminosities (L_{star}) have been collected from the literature using the references reported in Table 5, while the mass (M_{star}), and radius (R_{star}) were derived from the H-R diagram and the Siess et al. (2000) evolutionary tracks.

For multiple star systems the name we report in Table 5 is that of the primary star, which is the one with the earliest spectral type. However, in the table caption we list the separation of any other stellar companion within 10″ of the primary star. Given that the IRS/SH slit width is 4″.7, there are 15 objects with companions closer than 2″.5 that can contaminate the extracted IRS spectra. However, McCabe et al. (2006) show that only in 25% of the binary systems does the secondary flux becomes larger than the primary flux at wavelengths $>2\,\mu$m. Based on this, we assign the *Spitzer* spectrum always to the primary star in the 15 unresolved multiple systems.

We emphasize that the sample collected is biased in several ways: (1) the number of objects with sky observations and multiple on-source exposures (see Section 2), and (2) we only consider objects where the continuum has been detected and the S/N of continuum level is higher than 5. Hence, we do not attempt any statistical study based on this sample.

3.2. Accretion Properties

To test whether mid-IR H I lines trace the accretion shock region and/or the accretion flow, we compare H I line luminosities with stellar accretion luminosities (L_{acc}). One of the most direct methods to measure L_{acc} is through modeling of the UV excess continuum emission produced by the accretion shock (e.g., Gullbring et al. 1998). However, only 17 objects in our sample have such measurements (AA Tau, CS Cha, DE Tau, DK Tau, DN Tau, DM Tau, DR Tau, GM Aur, HN Tau, LkCa 15, RX 132207.2-693812, TW Hya, SZ Cha, Sz 27, LkHa 330, RX J1852.3-3700, and RX J1842.9-3532; see Ingleby et al. 2013 and Manara et al. 2014). To measure accretion luminosities in a consistent way for all the objects in our sample we will use the Hα line luminosity. Even if this method allows a homogeneous estimate of the accretion luminosity, we stress that the hydrogen lines in general, and the Hα line in particular, have several contributing mechanisms: accretion, stellar winds, jets, chromosphere (e.g., Hartmann et al. 1990; Calvet & Hartmann 1992). While this line is known to be an imperfect tracer of accretion in young stars, Rigliaco et al. (2012), among others, have shown that L_{acc} obtained from the UV excess emission and via indirect methods (e.g., Hα line luminosity) agree to within an order of magnitude.

To measure the accretion luminosity we first compute the Hα luminosity from the Hα equivalent width, the R- and/ or I-band magnitude, and the extinction (A_V) for each object (e.g., Hartigan et al. 1995). The data were dereddened using Mathis's reddening law for $R_V = 3.1$ (Mathis 1990). Next, we convert the Hα luminosity into L_{acc} using the relationship found by Rigliaco et al. (2012). Although this method provides self-consistent values for L_{acc} we are aware that the non-simultaneous observation of Hα, photometry, and A_V might introduce additional uncertainties in our estimates of L_{acc}. In Section 4.2 we describe how we account for these sources of uncertainty.

3.3. [Ne II] Line Fluxes and Luminosities

Water is largely detected in protoplanetary disks (e.g., Pontoppidan et al. 2010; Riviere-Marichalar et al. 2012), and its emission can contaminate other emission lines, as shown in the following sections. This is not the case for the [Ne II] line, which is quite isolated from other H_2O transitions. For this water-isolated and spectrally unresolved gas line we compute the flux by fitting a Gaussian profile to the observed line. We define the continuum level around the line as the mean value obtained sampling a 0.1 μm wide region shortward and longward of the transition, and the uncertainty on the measured flux is the rms in these regions. The line flux and the associated 1σ uncertainty are reported in Table 6 for each detection. In the same table we provide 3σ upper limits to the flux when [Ne II] lines are not detected. Line luminosities are then computed using the distances reported in Table 5.

We have compared the measured [Ne II] line fluxes (as reported in Table 6) with those reported by other authors using either different data reduction techniques (Pascucci et al. 2007; Lahuis et al. 2007; Espaillat et al. 2013), and/or including any possible unresolved contribution from other species (H_2O and OH; Carr & Najita 2011). We find that the measured line fluxes and upper limits are in agreement within the errors (see Figure 3).
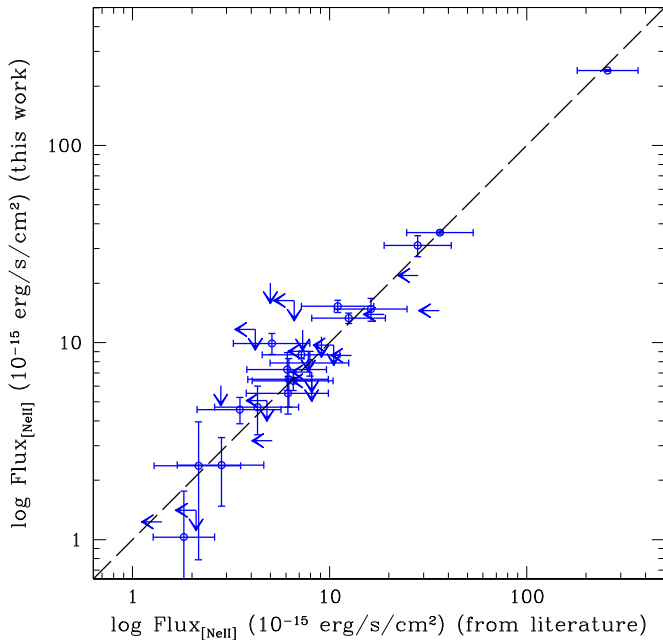
Figure 3. Comparison between the [Ne II] line fluxes measured following the data reduction chain explained in Section 2 and the line fluxes obtained from the literature using different data reduction techniques.

3.4. H I Line Fluxes and Luminosities

The method used to compute the [Ne II] line fluxes and luminosities could be in principle applied to the H I lines. However, because the H I (7–6) and H I (9–7) transitions are very close to water lines we must subtract any possible contamination from water before measuring line fluxes. We proceed as follows. In Section 3.4.1 we identify the objects that lack detectable water emission (hereafter, "water-free" disks[20]) and the objects where water is detected in their spectra ("water-contaminated" disks). For the water-free disks we compute line fluxes as in Section 3.3. For the water-contaminated disks we discuss a procedure to subtract water emission from the H I lines (Section 3.4.2) and then we measure the residual H I fluxes after water subtraction.

3.4.1. Water-contaminated versus Water-free Disks

To search for water emission in the source spectra we used the two water line complexes at 15.17 μm and 17.22 μm identified by Pontoppidan et al. (2010). These lines were selected because they are strong and more isolated than most other H_2O lines. Following Pontoppidan et al. (2010), we define as water contaminated those spectra in which both the H_2O lines are detected above 3σ. We do not find any case where one of the two lines is detected above 3σ, and the other one is not detected.

Among the 114 disks in our sample, 33 are water-contaminated. The remaining objects have water-free spectra. We show in Figure 4 a water-contaminated spectrum (DR Tau), and a water-free spectrum (DE Tau) in the region around the 15.17 μm and 17.22 μm water lines. For comparison we also show a synthetic water spectrum modeled assuming a gas temperature of 600 K and a water column density of 10^{18} cm^{-2} (see next section). Line fluxes, together with the uncertainties and continuum level next to the lines, are reported in Table 6.

---

[20] We note that these objects might possibly show water contribution in higher S/N or higher resolution spectra.
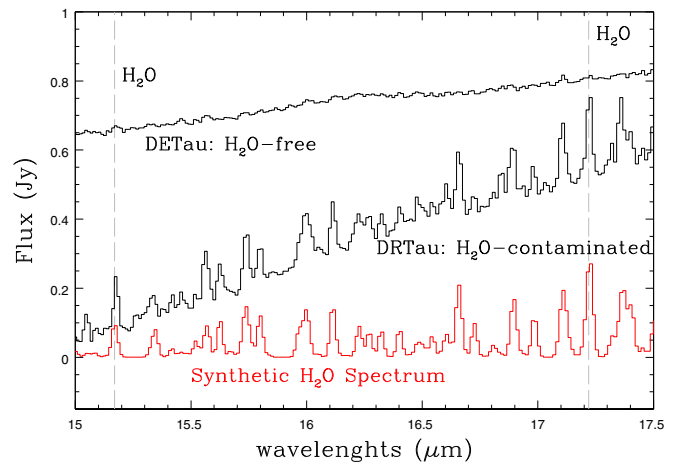

Figure 4. Examples of water-contaminated (DR Tau), water-free (DE Tau), and synthetic H_2O spectrum in the wavelength region around the two isolated H_2O lines at 15.17 and 17.22 μm. The target spectra are shown in black, and the synthetic water spectrum is shown in red.

3.4.2. Correcting for Water Emission

Water emission lines have been detected toward many protoplanetary disks using the *Spitzer*/IRS spectrograph (Pontoppidan et al. 2014 for a review). Previous studies have shown that a simple model, which assumes a plane-parallel slab geometry and gas in local thermal equilibrium (LTE), can reproduce the fluxes of the observed H_2O lines relatively well (e.g., Carr & Najita 2011). However, we are aware that these assumptions ignore the non-LTE effects and the complex geometric structure of disks (see Meijerink et al. 2009). We use this simple model as developed in Pascucci et al. (2013) to subtract any water contamination from the H I lines. The specific LTE model takes the molecular parameters from the HITRAN 2008 database (Rothman et al. 2009) and requires only four inputs: the gas temperature, the water column density, the radius of the emitting area, and the line width (which we assume to be the thermal line width, i.e., variable with temperature). We created a grid of synthetic spectra using five different gas temperatures ($T = [400, 500, 600, 700, 800]$) and water column densities ($N_{col} = [10^{17}, 5\times10^{17}, 10^{18}, 5\times10^{18}, 10^{19}$ cm$^{-2}]$) and assumed the same projected emitting area of radius 1 AU. The chosen inputs span the range of parameters inferred for the warm disk atmosphere of T Tauri stars (Carr & Najita 2011; Salyk et al. 2011).

The water lines contaminating the hydrogen lines are centered at $\sim$12.39 μm and $\sim$11.32 μm for the H I (7–6) and H I (9–7) transition, respectively. In the following we will refer to these lines as "H_2O-contaminating." To subtract off the water contribution to the observed H I lines we have searched the synthetic spectra for *isolated* H_2O lines with similar properties to the H_2O-contaminating ones. The two water lines that we have identified will be called in the following "H_2O-isolated" lines and have the following characteristics: they have similar lower energies (E_{low}) and Einstein A-coefficients (A_{ul}) (within 15% at most) as the H_2O-contaminating lines; H_2O-isolated line is within 1 μm from the corresponding contaminating line, so that the continuum level does not substantially change. Following these criteria we find that the H_2O-isolated line at 13.13 μm is the best match for the H_2O-contaminating line at 12.39 μm, while the H_2O-isolated at 11.97 μm has very similar properties as the H_2O-contaminating at 11.32 μm (see Table 2). We show in Figure 5 the ratio between the H_2O-contaminating/isolated
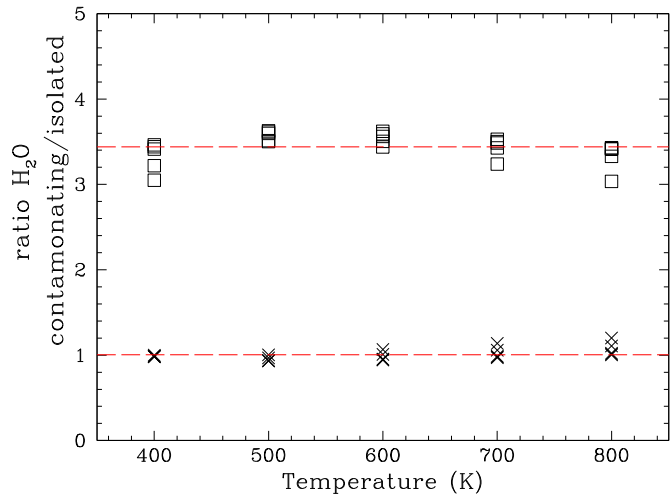
Figure 5. H_2O-contaminating/isolated line ratios: crosses for $H_2O(11.32\,\mu m)$/$H_2O(11.97\,\mu m)$ and squares for $H_2O(12.39\,\mu m)$/$H_2O(13.13\,\mu m)$. The ratios are computed for all the temperatures and column densities explored with the model grid. At each temperature there are five ratios, one for each value of the column density.

Table 2
H_2O Line Properties

Line	Wavelength (μm)	A_{ul} (s^{-1})	E_{low} (cm^{-1})
H_2O-contaminating	11.3241	1.576	2746.02
H_2O-contaminating	12.3962	7.665	3211.21
H_2O-isolated	11.9681	1.281	2629.33
H_2O-isolated	13.1325	6.788	3244.60

line fluxes for all the temperature and column density of the synthetic spectra. The ratios are quite constant among all the synthetic spectra, with $H_2O(12.39\,\mu m)$/$H_2O(13.13\,\mu m) \sim 3.5$ and $H_2O(11.32\,\mu m)$/$H_2O(11.97\,\mu m) \sim 1.0$, and vary within a factor of 1.5 at most over our grid of synthetic spectra.

Once we identified the best water proxies, we searched all the spectra for H_2O-isolated lines. In the SH-*Spitzer*/IRS spectra none of the 83 water-free spectra shows these lines, as expected because the H_2O lines become weaker at shorter wavelengths (e.g., Salyk et al. 2011). In the 33 water-contaminated disks, we subtracted the water contribution from the H I line fluxes as follows: if the H_2O-isolated line is detected above the 3σ level, we use it and its ratio to the nearby H_2O-isolated line to compute the H_2O-contaminating flux (as $H_2O(12.39\,\mu m) = 3.5\times H_2O(13.13\,\mu m)$ and $H_2O(11.32\,\mu m) = H_2O(11.97\,\mu m)$, respectively for H I(7–6) and H I(9–7)), and then subtract it from the measured H I line flux. If the H_2O-isolated line is not detected, we subtract its 3σ upper limit from the observed H I flux. After subtracting the water contamination from the observed line flux, we obtain the actual hydrogen line flux. The final line fluxes after water subtraction and errors are reported in Table 6. We also show in parentheses the total flux observed before subtracting the water contribution in the objects where the H I lines are detected. In the case of H I non-detections we provide the 3σ upper limit to the flux. Any other water contribution, if present, is within the 10% absolute flux uncertainty. As for the [Ne II], we have compared our H I(7–6) line flux measurements with the few already reported in the literature (Pascucci et al. 2007; Carr & Najita 2011). We find that the reported values are in agreement within the errors and the absolute flux uncertainty.

Table 3
Line Detections

Detected Lines	Total Number of Objects	Relative %		
		F	T	D
[Ne II]	49	67	31	2
H I(7–6)	46	57	26	17
H I(9–7)	11	55	27	18
[Ne II]+H I(7–6)	24	50	46	4
H I(7–6)+H I(9–7)	11	55	27	18
[Ne II]+H I(7–6)+H I(9–7)	6	50	50	0

Notes. The second column shows the total number of objects where the lines listed in Column 1 have been detected. The third, fourth, and fifth columns report the relative percent of these objects in full, transitional, and debris disks, respectively.

3.5. Line Detections Summary

We detect the [Ne II] line at $12.81\,\mu m$ in 49 objects in our sample. Among the 67 objects where the [Ne II] line is not detected, 37 are full disks, 4 are transitional disks, and 26 are debris disks. One debris disk has a [Ne II] line detection (E. Rigliaco et al., in preparation). After correcting for water contamination, we identify 46 objects with an H I(7–6) detection above 3σ, 11 of them also show the weaker H I(9–7) line. In six spectra we detect all three lines of interest: the [Ne II], the H I(7–6), and the H I(9–7) line. Line detections are summarized in Table 3. We note that all objects where water emission is detected are full disks and none of the transitional or debris disk spectra have detectable water emission. Thus, expanding upon previous results (e.g., Pontoppidan et al. 2010), our analysis shows that the absence of water lines in the SH module is typical to more evolved transitional and debris disks, while full disks can either have a water rich spectrum or not.

Interestingly, we detect H I(7–6) in eight young (<20 Myr) debris disks. We will discuss these objects in Section 4.5.

3.6. H I Lines versus Continuum Luminosity

Once we accounted for the water contribution and measured the H I(7–6) and H I(9–7) line luminosities, we investigated their behavior as a function of the continuum luminosity around the lines (Figure 6). As also seen in other IR lines ($H_2S(2)$, [Fe I] at $24\,\mu m$, [Ne II]; e.g., Lahuis et al. 2007), there is a correlation between the H I mid-IR lines and the continuum flux level next to the lines. This correlation could be influenced, but it is not exclusively driven, by the more favorable contrast between line and continuum luminosities where the continuum is lower (as demonstrated by finding the same increasing trend between the line to continuum versus continuum flux). We have also investigated this correlation for different disk morphologies and find that debris disks have lower H I line luminosities and continuum luminosities than transitional and full disks. In order to understand whether these differences are statistically significant we have measured the mean and standard deviation of line and continuum luminosities for the three different disk morphologies (shown as solid lines in Figure 6). From this analysis we conclude that, even if transitional disks appear having lower H I and continuum luminosities than full disks, their difference is within 1σ uncertainty, and thus not statistically significant. On the other hand, debris disks show consistently lower luminosities, both in the continuum and in the lines.
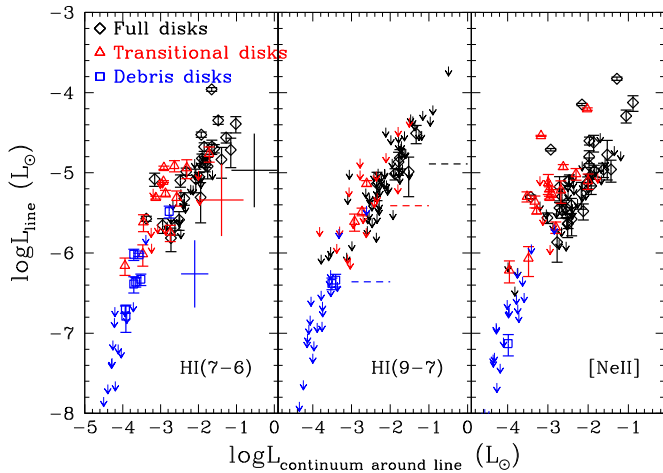
Figure 6. H I(7–6), H I(9–7), and [Ne II] line luminosity vs. continuum luminosity around the lines. Black diamonds represent objects surrounded by a full disk, red triangles are for transitional disks, blue squares for debris disks. Downward pointing arrows are upper limits. In the left panel solid lines represent the mean value of line and continuum luminosities with the 1σ uncertainty for the objects where both line and continuum are detected. In all cases, the mean value for the x-axis has been shifted by +1.5 for clarity. In the middle panel we show the mean in the line luminosity as dashed lines, given the large fraction of non-detections. We note again that the measure of the means is only based on the detections, and for the H I(9–7) lines the upper limits are more numerous than the detections.

4. DISCUSSION

4.1. Mid-IR H I Lines: Disk Tracers?

In the following we compare the [Ne II] line fluxes obtained from our reduction of the *Spitzer* spectra with those of the H I lines to test if these two lines could trace the same region in/around the disk. In particular, we test if [Ne II] and H I lines may trace the disk surface. As mentioned in Section 1, [Ne II] lines have been studied both with *Spitzer* and with ground-based spectrographs at higher spectral resolution. These studies have shown that the [Ne II] line mostly traces jets/outflows in high-accreting stars and the hot disk surface in lower accretors ($\dot{M}_{acc} \lesssim 5 \times 10^{-8}\, M_\odot$ yr^{-1}; e.g., Güdel et al. 2010; Sacco et al. 2012). Unfortunately, similar ground-based follow-up studies have not yet been carried out for the mid-IR H I lines, hence a direct comparison of high-resolution spectra cannot be done. The vast majority of the objects in our sample (namely, 85%) for which we have computed L_{acc} (and $\dot{M}_{acc}$) can be classified as "low accretors" according to the threshold value reported above (Güdel et al. 2010). Hence, for most of our sources a detection of [Ne II] in the *Spitzer* spectrum is most likely due to emission from the hot disk surface.

The left panel of Figure 7 shows a log–log plot of the H I(7–6) line luminosity at 12.37 μm versus the [Ne II] line luminosity at 12.81 μm. The luminosities of the two lines, when they are both detected, appear positively correlated, with a Pearson correlation coefficient of $\sim$ 0.9 and p-value $\sim 10^{-6}$. The correlation becomes weaker when upper limits are considered. However, this correlation could be affected by the underlying correlation between the line luminosities and the continuum luminosities around the line (see Figure 6 and discussion in Section 3.6). To account for this possible effect we plot in Figure 7 (right panel) the equivalent widths of the two observed lines. The [Ne II] and H I(7–6) equivalent widths do not show any obvious correlation, and the Pearson correlation coefficient drops to $\sim$0.4 (weak correlation) and the p-value $\sim$ 0.04. This result suggests that the positive relation between the H I(7–6) and [Ne II] line
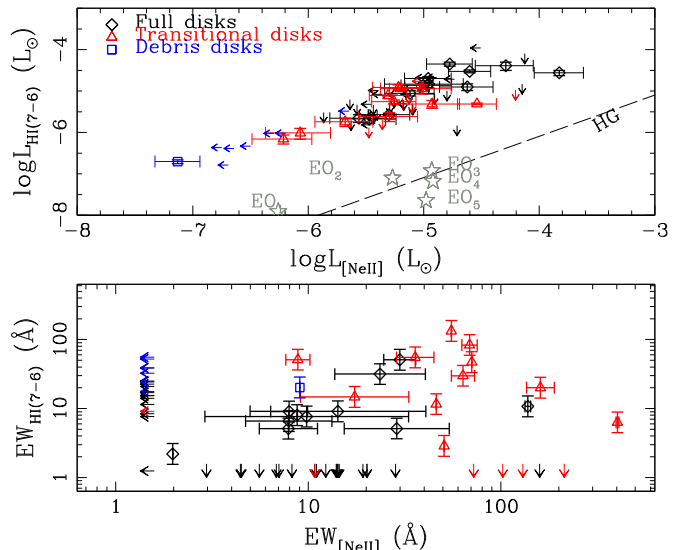

Figure 7. Top: H I(7–6) vs. [Ne II] line luminosity. We also show the prediction of these line luminosities for different theoretical models. The black-dashed line (labeled as HG) shows the H I(7–6)/[Ne II] line relation for a disk irradiated by EUV photons (Hollenbach & Gorti 2009). The gray stars refer to X-ray irradiated primordial disk with $\log L_X = 29.3$ (EO$_1$), $\log L_X = 30.3$ (EO$_2$), and transitional disks illuminated by $\log L_X = 30.3$ erg s^{-1} with inner hole 8.3 AU (EO$_3$), 14.2 AU (EO$_4$), and 30.5 AU (EO$_5$), as measured by Ercolano & Owen (2010). Bottom: comparison between the equivalent widths of the two lines.

luminosity is caused by the correlation between the line and nearby continuum.

To further test this finding, we compare the observed H I line luminosities with those predicted by models of disks irradiated by high-energy photons (Ercolano et al. 2008; Hollenbach & Gorti 2009; Ercolano & Owen 2010). In an EUV (13.6 eV$<$ $h\nu$ < 0.1 keV) irradiated disk the predicted $L_{HI(7-6)}/L_{[NeII]}$ ratios are as small as $\sim$0.008 (Hollenbach & Gorti 2009) because the radiative recombination rate of hydrogen is smaller than the electronic collisional excitation rate of [Ne II]. The observed line ratios are instead almost two orders of magnitude higher than the predicted ones (see Table 6). A disk irradiated also by X-rays ($h\nu > 0.1$ keV) still produces an H I(7–6) line luminosity more than one order of magnitude smaller than the ones observed (Ercolano et al. 2008; Ercolano & Owen 2010). The comparison between the observed line luminosity and different theoretical models shows that it is unlikely that the observed H I(7–6) lines trace the same hot disk atmosphere that produces the [Ne II] lines.

In summary, both the lack of correlation between the [Ne II] and the H I(7–6) equivalent widths and the comparison with model predictions suggest that the H I(7–6) line is not tracing the same disk region as the [Ne II] line, and that the H I lines are unlikely disk gas tracers.

4.2. Mid-IR H I Lines: Accretion Indicators?

Hydrogen recombination lines from the Balmer to the Paschen and Brackett series (in the UV, optical, and near-IR wavelengths) have been extensively studied over the years, and have been convincingly found to trace infalling material onto the star, as demonstrated by their broad line profiles consistent with gas at almost free-fall velocity onto the star (e.g., Alcalá et al. 2014). Nevertheless, these line profiles are also known to have other contributing mechanisms: stellar wind, jet, chromosphere. Recently, Salyk et al. (2013), using high-resolution
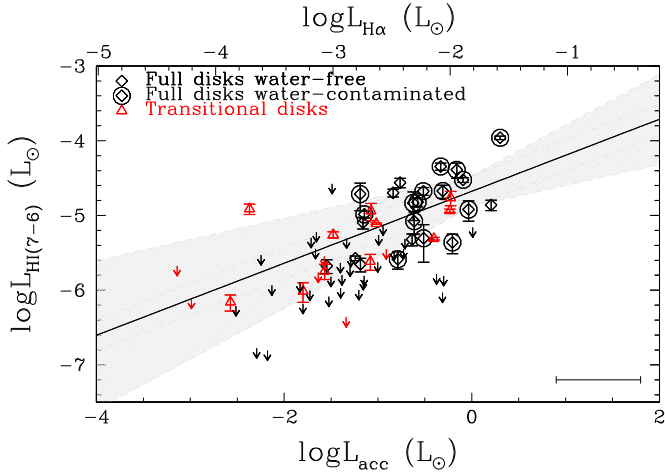
Figure 8. H I (7–6) line luminosity vs. Hα line luminosity and $L_{\rm acc}$. Circles are drawn around water-contaminated objects. The black-solid line shows the best linear regression line and the gray shaded area represents the approximate 95% confidence intervals (2σ) on the regression line. The typical error is shown in the bottom-right corner.
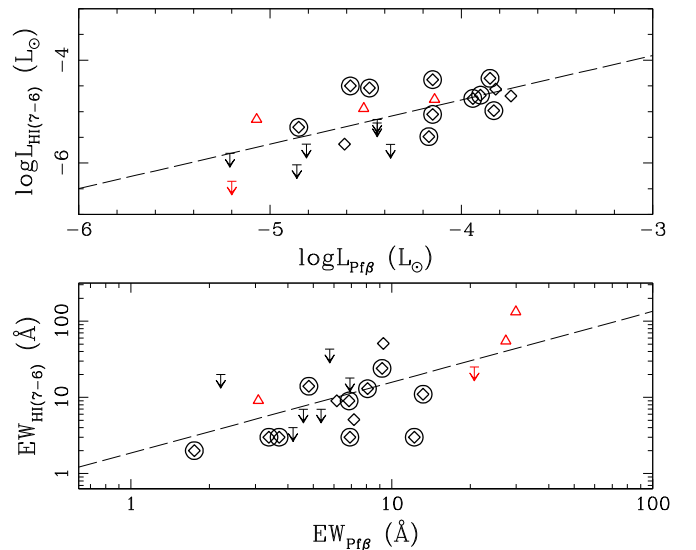

Figure 9. Top: H I (7–6) vs. Pfβ line luminosity. The black-dashed line shows the least-squares fit. Bottom: comparison between the equivalent widths of the two lines.

spectroscopy extended the accretion tracers to the Pfund series lines, including the Pfβ hydrogen recombination line at 4.65 μm (H I (7–5)).

To test if the H I mid-IR lines can be used as accretion indicators, in the rest of this section we focus on the subsample of full and transitional disks for which an estimate of the Hα equivalent width is available in the literature (see Table 5). We chose to use the H I (7–6) line (the strongest among the H I lines observed with the *Spitzer* SH module) to maximize the number of detected sources. Among the objects considered in this work, 73 have an estimate of the accretion luminosity from the Hα line (34 of those have an H I (7–6) detection).

We show in Figure 8 the H I (7–6) line luminosity as a function of the Hα line luminosity and the accretion luminosity measured as described in Section 3.2. There is a linear correlation between $\log L_{\rm HI(7-6)}$–$\log L_{\rm acc}$. To estimate the best fit regression line for the objects with detection in both quantities, and to account for the measured errors in both the *x*- and *y*-axes we employ the Bayesian method as implemented in the IDL routine *linmix_err* (Kelly 2007). The error on the *y*-axes is driven by the uncertainty on the observed line fluxes. The uncertainty in our estimate of $L_{\rm acc}$ is given by the combination of several factors: the uncertainty on the Hα equivalent width, the non-simultaneous observation of Hα, photometry, and extinction, the error on the extinction value (A_V), and the errors on slope and intercept of the $L_{\rm acc}$–$L_{\rm Hα}$ relationship. Following Costigan et al. (2012) we assume a mean amplitude of variation in the derived accretion luminosities of ∼0.37 dex, which includes Hα equivalent width uncertainties, time variability, and the error in the $L_{\rm acc}$–$L_{\rm Hα}$ relationship. We also consider an uncertainty on A_V of 1 mag (e.g., Edwards et al. 2013), which gives a final uncertainty on $L_{\rm acc} \sim 0.5$ dex. We find the following best fit regression line between the H I (7–6) line luminosity and the accretion luminosity:

$$\log L_{\rm HI(7-6)}/L_\odot = (0.48 \pm 0.09) \times \log L_{\rm acc}/L_\odot - (4.68 \pm 0.10).$$
(1)

We have checked that the $\log L_{\rm HI(7-6)}$–$\log L_{\rm acc}$ correlation is not driven by the distance and/or stellar luminosity dependence. We have also ascertained that the relationship between the luminosity of the H I (7–6) line and $L_{\rm acc}$ measured through UV-excess emission for only 15 objects (see Section 3.2)

lies within the 95% confidence intervals. We note that the uncertainty on the intercept we find in Equation (1) is similar to the those found using different H I lines (e.g., Alcalá et al. 2014), suggesting that the scatter around the fit is similar when using different H I lines. On the other hand, the slope found in Equation (1) is shallower than the ones found for the H I lines in the optical and near-IR wavelengths. This suggests that the MIR lines are less sensitive to accretion luminosity variations.

Knowing $L_{\rm acc}$ and the stellar properties we can also compute the mass accretion rate ($\dot{M}_{\rm acc}$) using the classical relation from Gullbring et al. (1998):

$$\dot{M}_{\rm acc} = \left(1 - \frac{R_{\rm star}}{R_{in}}\right)^{-1} \frac{L_{\rm acc} R_{\rm star}}{G M_{\rm star}},$$
(2)

where $R_{\rm in}$ is the radius at which the accreting gaseous disk is truncated due to the stellar magnetosphere. In full disks, $R_{\rm in}$ has been found ranging between $3 R_{\rm star}$ and $10 R_{\rm star}$ (Johns-Krull 2007), and usually $R_{\rm in} = 5 R_{\rm star}$ is assumed. In our sample we do not only consider full disks, but also transitional disks where the geometry of the gas disk around the star could be different. We do not speculate on how that could change for more evolved disks, and we will use the $R_{\rm in} = 5\,R_{\rm star}$ for all the different disk morphologies.

For the subsample of objects where the Pfβ line is detected (Salyk et al. 2013) and the H I (7–6) is detected and not water contaminated (this work) we find that their luminosities, as well as equivalent widths, are correlated with Pearson correlation coefficients ∼0.7 and ∼0.8, respectively, and p-value ∼ 0.007 and ∼0.05, respectively (Figure 9). While Salyk et al. 2013 report lower Pfβ luminosities and high EWs for five transitional disks with respect to full disks, we do not find any statistically significant difference in the H I (7–6) lines in our much larger samples of transitional and full disks (see also Section 4.1). We also note that these two samples do not have statistically different $L_{\rm acc}$, as also reported in other studies where $L_{\rm acc}$ are consistently derived (Keane et al. 2014, Fang et al. 2009).

The fact that the H I (7–6) line correlates both with the Hα and Pfβ lines suggests that the Humphreys α line at 12.37 μm is likely an accretion indicator, as the hydrogen lines belonging to other series (Hα (e.g., Muzerolle et al. 1998), Paβ (e.g., Folha
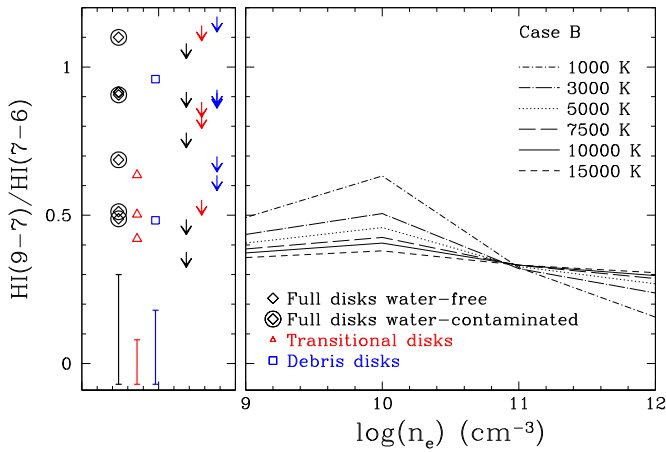
Figure 10. H I (9–7)/H I (7–6) line ratio vs. the electron density. Case B models for different temperatures as labeled. The range of the observed ratios is shown along the left side, where the typical uncertainties on the observed ratios are also plotted.

Figure 11. H I (9–7)/H I (7–6) line ratios vs. the hydrogen column density for the observed ratios. Kwan & Fischer models for different temperatures as labeled. Symbols as in Figure 10

& Emerson 2001), Brγ (e.g., Natta et al. 2006), and Pfβ (Salyk et al. 2013)).

Speculating on the correlation reported in Equation (1), we can measure what the mass accretion rates would be if the H I (7–6) lines in the debris disks spectra were accretion related. We find that debris disks with detected H I lines span the lower range of mass accretion rate (covering the range between $\times 10^{-10}$–$2 \times 10^{-12} \, M_\odot \, yr^{-1}$), as would be expected by their more evolved stage and the lack of gas in their disks.

4.3. H I Line Ratios

Hydrogen line ratios can be used as a diagnostic tool to constrain the physical conditions (density and temperature) of the emitting gas. Among the sample of objects analyzed in this paper, in 46 the H I (7–6) transition is detected above 3σ, and 11 of those show as well a detection of the H I (9–7) transition. The detected H I (9–7)/H I (7–6) line ratios range between ~0.4 and ~1.1. The upper limits cover a similar range. We can retrieve information on the physical properties of the emitting gas by comparing the observed ratios with those predicted by two different models: the Case B (Hummer & Storey 1987; Storey & Hummer 1995) and the Kwan and Fischer (Kwan & Fischer 2011, KF) models. In these models the H I line ratios ranges between ~0.3 and 0.5 in the optically thin regime, and become higher (between ~1.0 and 2.0) when the lines are optically thick.

4.3.1. Case B Models

The Case B model for radiative ionization and recombination (Baker & Menzel 1938) assumes that gas is optically thick to Lyman series photons and optically thin to photons associated to all other transitions. This model has been largely used to retrieve the properties of gas accreting onto T Tauri stars. However, results found considering individual objects and different hydrogen lines indicate very different physical properties of the accreting gas (Bary et al. 2008; Rigliaco et al. 2009; and Edwards et al. 2013 for a review). Using the interactive online server[21] (Hummer & Storey 1987; Storey & Hummer 1995), we computed the predicted line ratios for a range of temperatures from 1000 K to 15,000 K and electron densities from 10^9 to $10^{12} \, cm^{-3}$ (see Figure 10).
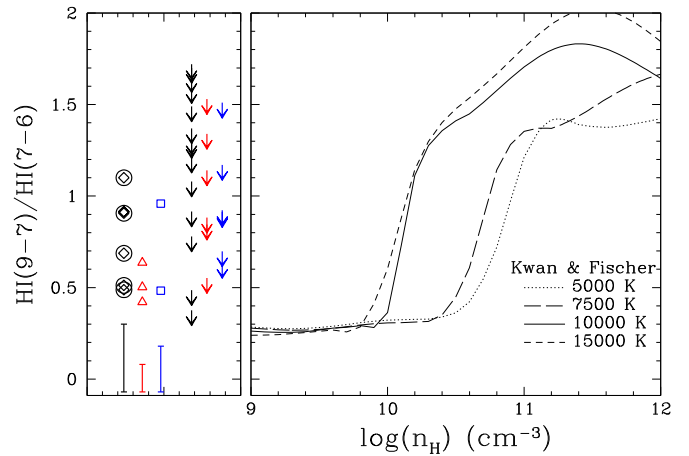
The predicted H I (9–7)/H I (7–6) line ratios are almost constant (between ~ 0.3 and 0.4) for $T \geqslant 5000$ K over the electron density range considered here. As the temperature decreases under 5000 K, the predicted ratio increases from ~0.3 to ~0.7 until electron densities $n_e \lesssim 10^{10} \, cm^{-3}$, and then decreases to ~0.2 when n_e becomes larger. Thus, a large range of temperatures, down to $T \sim 1000$ K, is required to explain most of the observed ratios. Still, ratios as high as 1.0 cannot be explained by the Case B models. In addition, as pointed out in Edwards et al. (2013), the necessity to maintain low line optical depths in the Case B models puts some restrictions to the applicability of this model to regions with high densities such as accretion funnels in YSOs.

4.3.2. Kwan and Fischer Models

Kwan & Fischer (2011) predicted hydrogen line ratios using a different approach than the Case B, in that they consider individual line optical depths. The inputs of these calculations are the gas temperature, the hydrogen density, the ionization rate (which was not specified in the case B models), and the velocity gradient with respect to the emission length scale (see Kwan & Fischer 2011 and Edwards et al. 2013 for more details). These parameters are chosen to replicate conditions in the region of winds and accretion flows in accreting YSOs.

We show in Figure 11 the comparison between the KF model predictions for the H I (9–7)/H I (7–6) line ratio and the observations.[22] The input gas temperatures span from 5000 K to 15,000 K, and given that the $(n_e)/(n_H)$ ratio is between 0.1 and 1.0, the hydrogen densities (n_H) cover similar electron densities to those shown in Figure 10 for the Case B models. The ratios suggested by the KF models are almost constant for all the temperatures until $n_H \sim 10^{10} \, cm^{-3}$. As the density increases, the line optical depth increases as well, first for the (7–6) transition, which explains the steep increase in line ratio. For $(n_H) > 10^{11} \, cm^{-3}$ both lines have large optical depths which explains the plateau. While the general behavior is similar for all temperatures, the specific transition density is ~$10^{10} \, cm^{-3}$ for $T \gtrsim 10,000$ K and ~$5 \times 10^{10} \, cm^{-3}$ for lower temperatures. Thus, unlike the Case B models, the KF models can explain all the observed line ratios with a limited range of temperatures
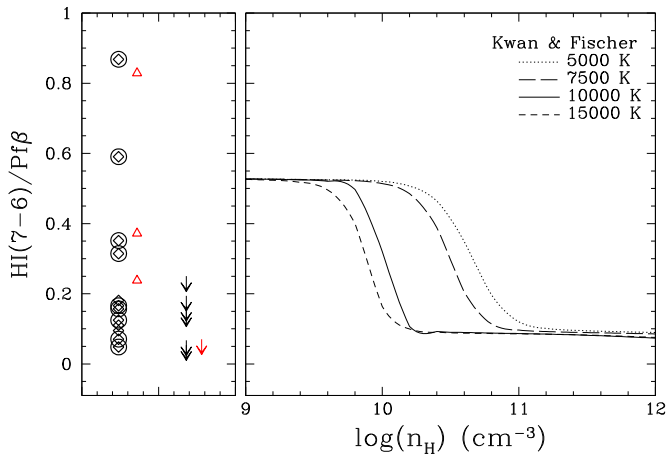

Figure 12. H I (7–6)/Pfβ line ratios vs. the hydrogen column density. Kwan & Fischer models for different temperatures as labeled. Same symbols as Figure 10.

(5000–15,000 K) and relatively narrow range of gas densities ($n_H \sim 10^{10}$–10^{11} cm^{-3}).

4.3.3. Comparison between Model Predictions and Gas Physical Properties

According to Martin (1996), who modeled the temperature and density profiles for gas channeled in magnetospheric accretion funnels, the typical temperatures in these regions are ~6000 K, and hydrogen densities are as high as 10^9–10^{10} cm^{-3}. Muzerolle et al. (2001), considering the Hα and Hβ lines, found that the temperature of magnetospherically accreting gas ranges between 6000 K and 12,000 K for a range of accretion rates between 10^{-6} and 10^{-10} $M_\odot$ yr^{-1}. Recently, Edwards et al. (2013) examined near-IR hydrogen line ratios for a sample of T Tauri stars. They find that the hydrogen density (n_H) in the line formation region is constrained within 2×10^{10}–2×10^{11} cm^{-3}, while the temperature is not well delineated.

If the hydrogen mid-IR lines are tracing accretion at least in full and transitional disks, the observed H I (9–7)/H I (7–6) line ratios cannot be explained by the gas properties predicted by the case B models. In fact, as we have seen is Section 4.3.1 and Figure 10 the observed line ratios require gas colder than 5000 K irrespective of the electron densities. Such physical properties, and in particular such low temperatures, are unlikely in the magnetospheric accretion columns, in which we expect temperature of at least a factor of two higher and a much narrower range in density (e.g., Muzerolle et al. 2001).

On the other hand, the KF models suggest gas properties that better match the scenario in which the mid-IR hydrogen lines are produced in the accretion funnels because they predict an hydrogen column density (n_H) between 10^{10} and 10^{11} cm^{-3}, and a temperature range between 5000 and 15,000 K (see Figure 11). The analysis of the H I (7–6)/Pfβ line ratios for the subsample of objects where these two lines have been observed adds additional constraints. In all but one object the observed line ratio is consistent with the KF model predictions for n_H between ~10^{10} and ~10^{11} cm^{-3} and $T > 5000$ K (see Figure 12). These results not only suggest that in most cases H I (7–6) and Pfβ might have a common origin, but that this origin is from hot gas with relatively high hydrogen column density (as expected in the accretion funnels). The objects where both H I (7–6) and Pfβ are detected, but the H I (7–6)/Pfβ line ratio does not fit the Kwan & Fischer models are VW Cha and TW Hya, where the H I (7–6)/Pfβ line ratios is ~0.9.

We note that similarly stringent constraints on the gas physical properties cannot be placed when using shorter wavelength hydrogen lines. In particular, we have analyzed model predictions (both case B and KF models) for the H I (7–6)/Hα and H I (7–6)/Paβ lines. We find that the observed ratios span a wider range of values, making the comparison with models inconclusive. This could be due to the different optical depths of the compared lines, which could affect the Hα line as well as other short wavelength transitions, or to time variability, which may be more pronounced at shorter wavelengths. In the case of the H I (7–6)/Hα line ratio we must also take into account that Balmer series lines in general, and Hα line in particular, have quite complicated profiles, with a variety of structures that include blueshifted absorption and line asymmetries (e.g., Basri & Batalha 1990).

4.4. Chromosphere and High-density Wind

The analysis carried out so far has shown that the H I mid-IR lines are very unlikely disk tracers. Moreover, the correlation between the H I (7–6) line and the accretion luminosity, and the H I line ratios support an origin of these lines in the accretion funnels for full and transitional disks. However, Hollenbach & Gorti (2009) discussed two other possibilities for the origin of H I mid-IR lines: an internal wind shock with high speed ($v_s \gtrsim$ 100 km s^{-1}) and close to the wind origin ($\lesssim 1$ AU), or the stellar chromosphere (see also Pascucci et al. 2007).

An internal shock origin, even if plausible for full disks, would be very difficult to reconcile with the detection of H I in the spectra of transitional and debris disks. Transition disks rarely show signs of outflows activity (see for example the optical forbidden line profiles in Hartigan et al. 1995), and debris disks have already dispersed most of their gas disk mass (e.g., Pascucci et al. 2006). While it is possible that mid-IR hydrogen lines trace different environments depending on the stellar/disk evolutionary stage, as shown for the [Ne II] line (see Section 1), a wind shock origin cannot explain the detections in transitional and debris disks.

The mean chromospheric electron density in T Tauri stars is $n_e \sim 10^{11}$ cm^{-3} (Giampapa et al. 1981, or $10^{11} \lesssim n_H \lesssim 10^{12}$ cm^{-3} if $0.1 < (n_e)/(n_H) < 1$; see Section 4.3.2). According to the KF model at these high densities the H I (7–6) and (9–7) transitions would be both optically thick, hence line ratios should be $\gtrsim 1$. Only few sources in our sample sport such large line ratios. Another way that we have employed to investigate the chromospheric origin of the H I lines is to consider the effect of the chromospheric emission on the measured accretion luminosity. Manara et al. (2013), quantified this effect by analyzing a sample of high dispersion spectra of non-accreting low-mass T Tauri stars. Measuring the Hα emission in non-accreting stars, and converting this value into an accretion luminosity, they find that the chromospheric activity can significantly contribute to the measured accretion luminosity when the latter is smaller that 10^{-3} $L_\odot$, and that this contribution is strongly dependent on the object's effective temperature (hence spectral type). They derive a correlation between $T_{\rm eff}$ and $L_{\rm acc,noise}$ (the latter representing the chromospheric contribution to the accretion luminosity). Unfortunately, their sample is limited to objects with spectral type in the range K7–M9.5, and none of our debris disks falls in this range. In the following we will focus on the 42 objects with $T_{\rm eff} < 4100$ K and with an estimate of $L_{\rm acc}$ (see Table 5). In Figure 13 we plot $L_{\rm acc,noise}$ obtained using the correlation provided by Manara et al. (2013, their Equation (2)) versus $L_{\rm acc}$ as reported in Table 5. Thirteen of these objects also show a
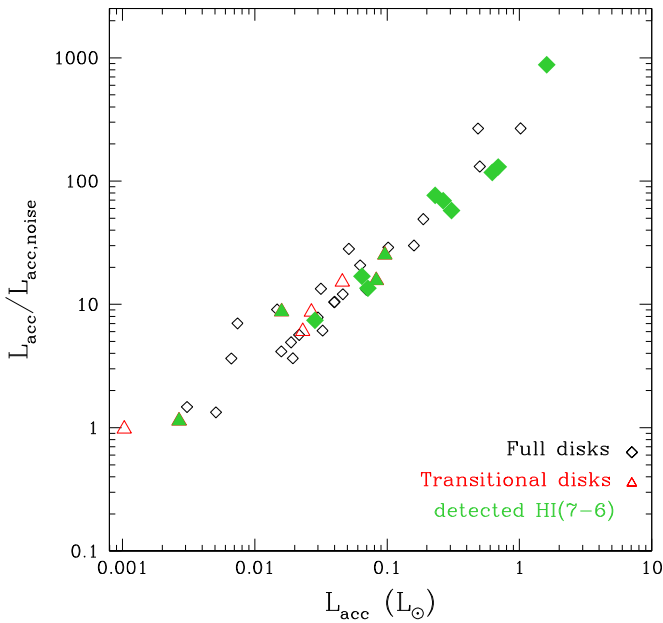
Figure 13. Contribution to the accretion luminosity from chromospheric emission ($L_{acc}/L_{acc,noise}$), measured using the relation found by Manara et al. (2013), vs. L_{acc} for all the objects with $T_{eff} < 4100$ K. Symbols are as labeled. Filled symbols refer to objects where H I (7–6) is detected.

detection in the H I (7–6) line (green-filled symbols). There is a small number of targets, where the ratio is not more than 5, for which the chromospheric contribution could substantially influence the estimate of the accretion luminosity. However, in the majority of objects L_{acc} is at least five times bigger than its chromospheric contribution, meaning that the latter is well within the estimated uncertainty on L_{acc}. Moreover, the objects where the H I (7–6) line is detected (identified as green-filled symbols in Figure 13) span all over the range of L_{acc}.

We can only test the chromospheric contribution over the accretion luminosity for ~40% of the total sample, where $T_{eff} < 4100$ K. For this subsample the previous analysis suggests that the H I lines are not contaminated by the chromospheric contribution at a significant level. We could not extend this analysis to objects with higher temperatures (earlier spectral types) and to debris disks. *It is possible that the H I mid-IR lines are tracing accretion in less evolved objects, while their contribution is only chromospheric in later evolutionary stages.*

The way to discriminate between accretion funnels, chromosphere, and high-density wind is through ground-based high-resolution (10–20 km s^{-1}) spectroscopy. In fact, for H I lines originating in accreting gas we will observe broad lines (FWHM~ 100 km s^{-1}; Muzerolle et al. 2001) close to the stellar velocity. A chromospheric component will be narrower (~40 km s^{-1}) and centered at the stellar velocity (e.g., Herczeg et al. 2007). An internal shock origin will instead produce H I profiles that are as broad as 100 km s^{-1} and can be also blueshifted by the same amount.

4.5. A Closer Look at the Debris Disks

As already mentioned in the previous sections, this paper reports the first detection of H I (7–6) and H I (9–7) gas lines in debris disks (we also detect the [Ne II] gas line in the *Spitzer* spectrum of HD 35850, as will be discussed in E. Rigliaco et al., in preparation). We show in Figure 14 a compilation of the eight debris disks line profiles where the H I (7–6) line has been detected. In the following we will investigate the properties
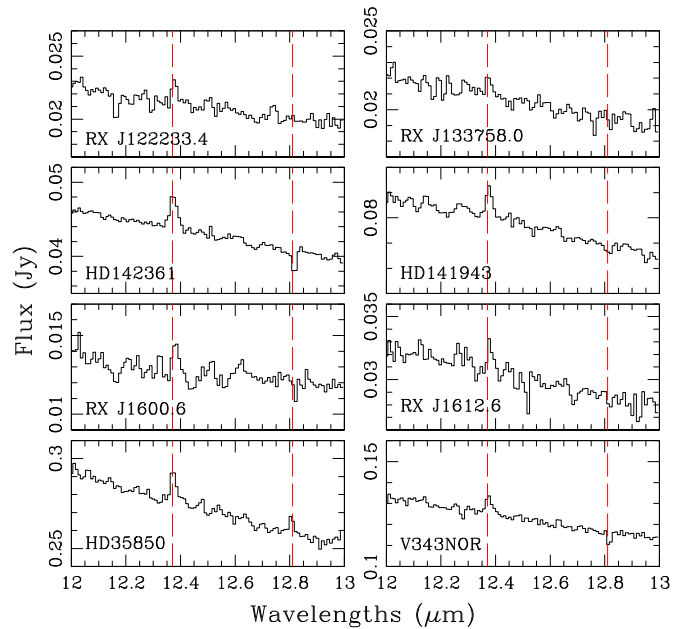
Figure 14. *Spitzer* spectra of the eight debris disks where the H I (7–6) line is detected.
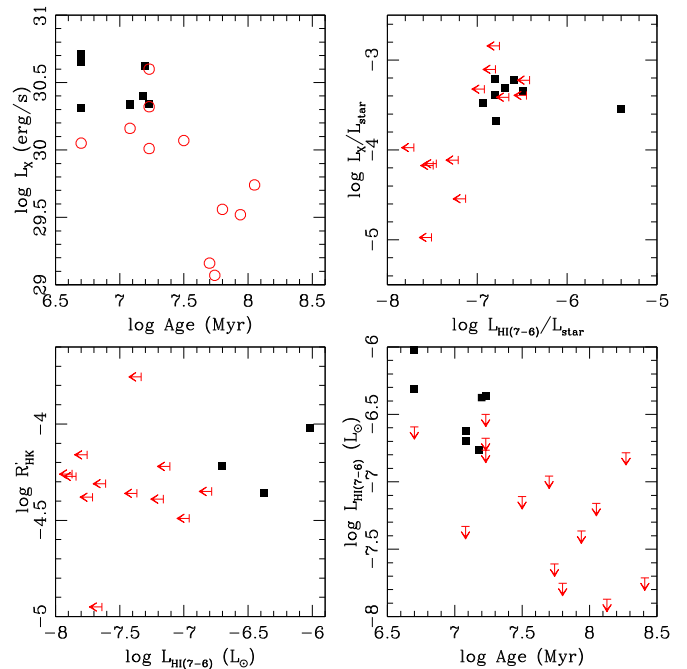
Figure 15. Top-left panel: X-ray luminosity vs. age. Black squares and red open circles refer to objects with detected and not-detected H I (7–6) line, respectively. Top-right panel: L_X/L_{star} vs. $L_{HI(7-6)}/L_{star}$. Bottom-left panel: chromospheric activity diagnostic R'_{HK} vs. the H I line luminosity. Bottom-right panel: H I (7–6) line luminosity vs. age.

of all the debris disks we have re-reduced, either with detected H I (7–6) lines or not (as reported in Tables 5 and 6). All these debris disks are observed within the FEPS[23] *Spitzer* Survey (Meyer et al. 2006), and we collect the quantities plotted in Figure 15 and reported in Table 4 from the FEPS Database.[24]

---

[23] Formation and Evolution of Planetary Systems
[24] http://feps.as.arizona.edu/index.html

Table 4
Debris Disks Properties

Name	Age (Myr)	log L_X (erg s^{-1})	R'_{HK}	Ref.
1RXS J121236.4-552037	17	30.32	. . .	6, 2
1RXS J122233.4-533347	17	30.34	. . .	6, 2
1RXS J130153.7-530446	17	30.01	. . .	6, 2
HD 119269	17	30.60	. . .	6, 2
1RXS J133758.0-413448	15	30.40	. . .	6, 2
1RXS J161458.0-275013	5	30.05	. . .	7, 2
HD 142361	5	30.71	-4.02	7, 2, 8
RXJ1600.6-2159	5	30.31	. . .	7, 2
RXJ1612.6-1859	5	30.65	. . .	7, 2
HD 35850	12	30.34	-4.22	10, 2, 9
V343Nor	12	30.33	. . .	10, 2
HD 19668	257	. . .	-4.38	2, 9
HD 25457	112	29.74	-4.39	5, 2, 9
HD 37484	50	29.16	-4.49	2, 2, 8
HD 12039	63	29.56	-4.16	2, 2, 8
HD 202917	32	30.07	-4.22	2, 2, 9
HD 141943	16	30.62	-4.36	2, 2, 4
HD 377	87	29.52	-4.36	2, 2, 9
HD 17925	55	29.07	-4.31	2, 2, 1
HD 32297	. . .	. . .	. . .	
HD 61005	135	. . .	-4.26	2, 4
HD 69830	1860	. . .	-4.95	9, 9
HD 134319	186	. . .	-4.35	9, 9
HD 216803	400	28.33	-4.27	2, 2, 4
AO Men	12	30.16	-3.75	10, 2, 3

References. (1) Baliunas et al. 1996; (2) FEPS Database; (3) Gray et al. 2006; (4) Henry et al. 1996; (5) Luhman et al. 2005; (6) Mamajek et al. 2002; (7) Preibisch et al. 2002; (8) White et al. 2007; (9) Wright et al. 2004; (10) Zuckerman et al. 2001.

We first investigate a chromospheric nature for the mid-IR hydrogen lines. As shown in Figure 15 (top-left panel), all the debris disks where the H I (7–6) line is detected are younger and with higher X-ray luminosity. The latter is a chromospheric indicator of magnetic activity (e.g., Feigelson et al. 2007), and its decay with age could let us conclude that the H I line in debris disks are chromospherical, and as the magnetic activity decreases (with age) they are no longer detected in older disks. Moreover, the X-ray emission of the debris disks with detected H I (7–6) lines almost reaches the saturation level for chromospheric emission ($L_X/L_{star} \sim 10^{-3}$; e.g., Patten & Simon 1996; Figure 15, top-right panel). This saturation level indicates that the chromospheric radiation emitted from the star cannot exceed a given fraction of the total stellar flux, and this limit is almost reached in all the observed debris disks, favoring again a chromospheric origin of the H I lines. Another test to check whether or not H I lines in debris disks are from chromospheric activity is shown in the bottom-left panel of Figure 15, where we plot the stellar chromospherical activity indicator R'_{HK} (collected from White et al. 2007). This indicator measures the core emission in the Ca II H and K lines, and the larger the value, the more chromospherically active the star (Noyes et al. 1984).[25] For the debris disks where this value has been measured there is no significant difference in terms of range covered by R'_{HK} as a function of H I line luminosity, showing that stars with the same chromospheric activity (similar R'_{HK} value) may or may not have a detected H I line. On the other hand, the object with strongest

---

[25] We note to the reader that the R'_{HK} index may itself vary with time along the magnetic cycle of the star.

H I line has the largest R'_{HK} value, which would support a chromospheric origin in this case. However, the sample is limited to only three objects, and statistical studies are not possible.

We also speculate on the possibility that, as for full and transitional disks, the detection of the mid-IR H I lines in the *Spitzer* spectra of debris disks might trace accretion at very low levels. In fact, Figure 15, bottom-right panel shows that the H I line is detected in the youngest systems from our sample, for which a low level of accretion may be still ongoing. While multiplicity studies are not complete for debris disks, it is intriguing to note that the two debris disks with a confirmed companion close enough to contribute to the observed *Spitzer* spectrum (see Table 5 in the Appendix) have mid-IR hydrogen line detections. This raises yet another possibility that the H I (7–6) line observed in debris disks is due to an accreting or chromospherically active companion, instead of the debris disk object itself. However, this remains a speculation at this point given the low number of detections.

In summary, even if a chromospheric origin appears the most likely based on the tests carried out so far, accretion cannot be ruled out. Only higher spectral resolution will be able to pin down the origin of mid-IR hydrogen lines.

5. SUMMARY AND OUTLOOK

We have re-reduced archival *Spitzer*/IRS spectra of 114 objects in different evolutionary stages, from full to transitional to debris disks, and we have investigated the origin of the H I mid-IR lines. Our main findings are as follows.

1. After correcting for the disk water contamination, we detect H I (7–6) line in 26 full disks, 12 transitional, and 8 debris disks. The fainter H I (9–7) line is detected in six full, three transitional, and two debris disks.
2. We find H I (7–6) luminosities similar to the [Ne II] 12.81 μm luminosities. These large luminosities exclude that the H I (7–6) line traces the same hot disk surface probed via the [Ne II] line.
3. Case B models cannot reproduce the observed H I (9–7)/ H I (7–6) ratios except for $T < 3000$ K. On the other hand, KF models reproduce the observed ratios for reasonable assumption of temperatures and hydrogen column densities (n_H). Using the KF models the n_H is fairly well constrained between $10^{10} < n_H < 10^{11}$ cm^{-3} but the temperature is not.
4. For the subset of full and transitional disks we report a positive correlation between the H I (7–6) line luminosity and the accretion luminosity. This trend, together with the results shown in point 3, suggests an origin of these lines from gas accreting onto the star.
5. A pure chromospheric origin of the mid-IR H I lines, can only be tested for sources with $T_{eff} < 4100$ K (40% of the total sample). For this subset of objects we find that the majority of them are not contaminated by chromospheric emission at a significant level.
6. We report the first detection of H I lines in *Spitzer* spectra of debris disks, which occurs only in the youngest systems studied here (<20 Myr). A chromospheric origin of these lines seems likely, but it is not possible to definitively rule out either a long-lasting accretion signature nature or the presence of a non-resolved accreting companion.

Ground-based high-resolution spectroscopy will enable the testing of this origin. Extending accretion indicators at mid-IR wavelengths may enable measuring mass accretion rates in

Table 5
Source Properties

Name	Association	Distance (pc)	SpTy	A_V	T_{eff} (K)	M_{star} ($M_\odot$)	L_{star} ($L_\odot$)	R_{star} ($R_\odot$)	HαEW (Å)	L_{acc} ($L_\odot$)	Reference
					Full disks						
IC348-2	IC 348	315	A2	3.8	8970	2.80	57.1	3.1	. . .	. . .	18, 11
IC348-6	IC 348	315	G3	3.9	5830	2.40	16.6	4.0	. . .	. . .	18, 11
IC348-31	IC 348	315	G6	8.6	5700	1.60	5.00	2.3	. . .	. . .	18, 11
IC348-37	IC 348	315	K6	2.8	4200	0.90	1.30	2.2	. . .	. . .	18, 11
IC348-55	IC 348	315	M0.5	8.5	3850	0.60	1.00	2.2	. . .	. . .	18, 11
IC348-68	IC 348	315	M3.5	2.1	3740	0.30	0.50	2.0	. . .	. . .	18, 11
04216+2603	Taurus	140	M0	. . .	3500	0.28	0.02	0.3	. . .	. . .	14, 21
04385+2550	Taurus	140	M0	9.3	3850	0.57	3.67	4.0	20.0	0.50	14, 21
AA Tau*	Taurus	140	K7	0.9	4060	0.73	1.38	2.3	37.1	0.07	14, 9
BP Tau	Taurus	140	K7	0.5	4060	0.73	1.62	2.4	40.1	0.07	14, 9
CW Tau*	Taurus	140	K3	2.2	4730	1.15	0.76	1.3	134.6	0.30	14, 49
CX Tau	Taurus	140	M2.5	0.8	3490	0.36	0.62	2.0	19.8	0.003	14, 9
CY Tau*	Taurus	140	M1	0.9	3705	0.47	0.71	1.9	69.5	0.06	14, 9
DD Tau ^{m,*}	Taurus	140	M3	0.4	3415	0.29	0.13	1.0	181.8	0.05	14, 49, 9
DE Tau	Taurus	140	M1	1.6	3705	0.46	1.47	2.8	54.0	0.23	14, 49, 9
DG Tau	Taurus	140	K6	1.4	4205	0.92	1.15	1.9	84.0	0.17	14, 49
DK Tau ^{m,*}	Taurus	140	K7	1.4	4060	0.74	1.32	2.2	19.4	0.02	14, 9, 44
DH Tau*	Taurus	140	M0	1.0	3850	0.56	0.76	1.8	53.4	0.03	14, 9
DL Tau*	Taurus	140	K7	2.0	4060	0.75	1.16	2.2	105.0	0.62	14, 49
DN Tau*	Taurus	140	M0	0.4	3850	0.55	1.62	2.7	11.9	0.016	14, 49
DO Tau*	Taurus	140	M0	2.2	3850	0.56	1.05	2.2	100.0	0.19	14, 49
DP Tau ^{m,*}	Taurus	140	M0.5	0.9	3850	0.56	0.85	1.9	85.4	0.05	14, 9
DQ Tau ^{a,*}	Taurus	140	M0	0.5	3850	0.56	0.93	2.0	112.9	0.04	14, 9
DR Tau*	Taurus	140	K5	0.5	4350	1.16	0.96	1.9	106.0	0.49	14, 49
DS Tau*	Taurus	140	K5	0.9	4350	1.10	0.68	1.3	58.7	0.16	14, 49
FM Tau*	Taurus	140	M0	0.9	3850	0.57	0.52	1.5	70.9	0.02	14, 9
FN Tau	Taurus	140	M5	1.4	3125	0.22	0.79	2.8	24.7	0.007	14, 9
FT Tau*	Taurus	140	M3	3.8	3415	0.31	0.16	1.0	254.3	0.49	14, 9, 40
FZ Tau*	Taurus	140	M0	2.7	3850	0.57	0.50	1.4	200.0	0.26	14, 49
HK Tau ^{m}	Taurus	140	M0.5	3.0	3850	0.56	1.12	2.2	29.3	0.028	14, 9,
HN Tau ^{m,*}	Taurus	140	K5	1.2	4350	0.78	0.22	0.8	163.0	0.15	14, 49
IP Tau	Taurus	140	M0	0.5	3850	0.59	0.17	0.9	11.0	0.005	14, 49
RW Aur ^{m,*}	Taurus	140	K3	0.4	4730	1.48	1.60	1.8	76.0	0.924	14, 49
SU Aur	Taurus	140	G2	0.9	5860	1.85	8.90	2.7	3.5	0.14	14, 9
UY Aur ^{m}	Taurus	140	K7	1.1	3850	0.60	0.91	2.1	72.8	1.02	14, 9, 49
AS 353A ^{m}	Perseus	150	M3	2.1	3415	0.32	0.68	2.2	124.5	1.60	38, 9
LkHa326	Perseus	250	M0	3.1	3800	0.49	0.05	0.5	52.7	0.10	6, 9
2071-H13/ NGC 2068	NGC 2068	400	K1	2.9	5080	1.68	2.63	2.0	36.7	0.42	11
2071-S1/ NGC 2068	NGC 2068	400	K4	4.1	4600	1.60	4.10	3.1	3.7	0.005	11
RX J1111.7-7620 ^{m}	Cha	160	K1	1.5	5080	1.78	3.09	2.2	7.6	0.04	43, 48
SX Cha ^{m,*}	Cha	160	M0.5	1.1	3850	0.57	0.61	1.6	33.2	0.02	15, 16
SZ50	Cha	160	M3	2.1	3350	0.90	0.78	2.5	46.0	0.015	15, 20
TWCha	Cha	160	M0	1.2	3850	0.56	3.10	3.7	28.3	0.04	15, 16
VW Cha ^{m,*}	Cha	160	K5	2.4	4350	1.14	4.02	3.3	71.7	0.81	15, 42
VZ Cha*	Cha	160	K6	0.5	4205	0.93	0.84	1.6	71.4	0.099	15, 42
WX Cha ^{m,*}	Cha	160	K7	2.1	4060	0.77	0.77	1.8	65.5	0.07	15, 1
XX Cha ^{m,*}	Cha	160	M2	0.6	3560	0.37	0.18	1.1	133.5	0.03	15, 1
Hen-3-600A	TWHya	56	M3	0.0	3415	0.26	0.06	0.6	21.8	0.007	46
TWA10	TWHya	100	M2	0.0	5500	0.90	0.60	1.0	. . .	. . .	55
1RXS J132207.2-693812	LCC	86	K1	0.6	5035	1.23	1.14	1.4	19.5	0.07	43, 8
EX Lup*	Lupus	190	M0	0.0	3850	0.55	1.31	2.4	31.3	0.06	26, 42
GQ Lup*	Lupus	190	K7	0.4	4060	0.76	4.53	4.1	31.7	0.31	26, 42
HT Lup ^{m}	Lupus	190	K3	0.0	4730	1.85	4.00	2.8	7.3	0.11	26, 42, 54
RU Lup*	Lupus	190	K7	0.7	4060	0.74	1.28	2.2	136.0	0.69	26, 42
1RXS J161411.0-230536 ^{m}	Upper Scorpius	140	K0	1.1	5250	1.62	2.95	2.0	. . .	. . .	43, 29
HD 143006	Upper Scorpius	169	G7	0.6	5800	1.12	3.30	1.7	10.7	0.19	43, 29
DoAr 24E ^{m,*}	ρOphiucus	160	G7	6.1	5630	2.15	10.75	3.3	7.1	0.24	15, 53
f DoAr 25*	ρOphiucus	160	K5	1.2	4350	1.11	2.19	2.3	12.0	0.05	8, 53
SR21 ^{m}	ρOphiucus	125	G2.5	9.0	5950	2.67	28.0	4.7	. . .	. . .	38
WaOph6*	ρOphiucus	160	K6	1.0	4205	0.90	1.46	2.3	35.0	0.02	26, 47
Ced110-IRS4	ρOphiucus	160	K2	. . .	4800	0.85	0.40	0.9	. . .	. . .	37
Ced110-IRS2	ρOphiucus	160	K3	3.3	4730	2.23	9.64	4.4	. . .	. . .	15
Haro 1-16*	ρOphiucus	160	K3	1.2	4730	1.80	3.39	2.7	59.0	0.24	14, 9
RNO 90*	ρOphiucus	160	G5	1.0	5770	1.28	2.74	1.6	76.0	0.47	26, 28
EC 82	Serpens	415	K7	1.0	4060	0.75	3.21	3.3	8.0	0.03	26, 9

Table 5
(Continued)

Name	Association	Distance (pc)	SpTy	A_V	$T_{\rm eff}$ (K)	$M_{\rm star}$ ($M_\odot$)	$L_{\rm star}$ ($L_\odot$)	$R_{\rm star}$ ($R_\odot$)	HαEW (Å)	L_{acc} ($L_\odot$)	Reference
Full disks											
RX J1842.9-3532	CrA	136	K2	1.1	4900	1.33	1.29	1.5	27.2	0.06	43, 51
RX J1852.3-3700	CrA	136	K3	1.0	4730	1.27	1.00	1.5	27.4	0.06	43, 8
V1331Cyg	Cyn	550	G8	0.0	5500	2.81	21.0	4.8	48.4	2.01	9, 35
Transitional disks											
IC348-21	IC 348	315	K0	4.7	5250	1.60	3.80	2.4	6.4	0.08	11
IC348-67	IC 348	315	M0.75	2.0	3720	0.50	0.50	1.8	32.5	0.03	11
IC348-72	IC 348	315	M2.5	3.0	3580	0.40	0.70	2.1	2.0	0.0007	11
IC348-133	IC 348	315	M5	3.6	3200	0.20	0.20	1.5	...	...	11
DM Tau	Taurus	140	M1	0.0	3705	0.47	0.37	1.3	138.7	0.046	14, 21
FP Tau	Taurus	140	M5	0.3	3125	0.22	0.62	2.5	38.5	0.001	14, 21
GM Aur	Taurus	140	K3	1.2	4730	1.27	1.00	1.5	96.5	0.58	14, 21
LkCa 15^m	Taurus	140	K5	1.0	4300	1.06	0.74	1.5	13.0	0.027	14, 21
St 34^m	Taurus	140	M3	0.2	3415	0.24	0.01	0.3	51.6	0.016	26, 50
UX Tau A^m	Taurus	140	K5	0.3	4350	1.17	0.91	1.9	9.5	0.03	14, 17
V836Tau	Taurus	140	K7	0.9	4060	0.81	0.34	1.2	55.0	0.16	14, 21, 34
LkHa 330	Perseus	250	G3	1.8	5830	1.25	2.78	1.5	20.3	0.59	3, 13
2071-H9/ NGC 2068	NGC 2068	400	K2	1.6	5250	1.41	2.03	1.7	1.2	0.004	11
CHX 22 (T54)^m	Cha	160	G8	1.2	5520	1.69	4.63	2.2	...	...	15, 48, 34
CS Cha	Cha	160	K6	0.8	4205	0.90	1.50	2.3	54.3	0.39	15, 42
SZ Cha^m	Cha	160	K0	1.9	5250	1.40	1.90	1.7	...	...	15, 42
Sz 18 (T25)	Cha	160	M2.5	1.6	3560	0.38	0.32	1.4	8.0	0.003	15, 30
Sz 27 (T35)	Cha	160	K8	3.5	4060	0.80	0.47	1.2	100.0	0.08	15, 30
TW Hya	TWHya	56	M0	1.0	3850	0.57	0.64	1.7	194.0	0.09	4, 42
IM Lup	Lupus	190	M0	0.7	3850	0.56	3.52	3.9	4.7	0.02	36, 42
DoAr 21	ρOphiucus	160	K1	6.6	5080	2.20	27.3	6.7	1.5	0.12	33, 31
Debris disks											
1RXS J121236.4-552037	LCC	108	K0	0.2	5150	0.90	0.50	0.9	...	...	5, 7
1RXS J122233.4-533347	LCC	124	G0	0.3	5860	1.24	2.23	1.3	...	...	5, 7
1RXS J130153.7-530446	LCC	108	K2	0.2	4700	0.82	0.30	0.8	...	...	5, 7
HD119269	LCC	85	G4	0.1	5700	1.07	1.31	1.2	...	...	5, 7
1RXS J133758.0-413448	UCL	98	K0	0.3	5250	0.90	0.68	0.9	...	...	5, 7
1RXS J161458.4-27501	Upper Scorpius	114	G5	0.6	5250	0.90	0.70	1.0	...	...	43, 8
HD 142361^m	Upper Scorpius	101	G3	0.5	5830	1.72	7.12	2.5	...	...	5, 7
RX J1600.6-2159	Upper Scorpius	160	G9	0.8	5410	1.66	3.77	2.1	...	...	43, 8
RX J1612.6-1859^m	Upper Scorpius	127	K0	1.5	5250	1.50	2.40	1.8	...	...	19, 8
HD 35850	βPictoris	26.5	F7	0.0	6000	1.20	1.78	1.2	...	...	5, 7
V343 Nor^m	βPictoris	38	K0	0.0	5250	0.90	0.67	0.9	...	...	5
HD19668	AB Dor	40	G8/K0	0.0	5500	0.90	0.60	0.8	...	...	5, 7
HD25457	AB Dor	19	F7	0.2	6000	1.20	2.50	1.5	...	...	5, 7
HD37484	Columba	60	F3	0.1	6740	1.30	3.90	1.5	...	...	5, 7
HD12039^m	Tuc-Hor	42	G4	0.2	6000	1.00	1.00	0.9	...	...	5, 7
HD202917	Tuc-Hor	46	G7	0.1	5750	0.90	0.70	0.8	...	...	5, 7
HD 141943	Field	67	G0	0.1	6030	1.55	6.19	2.2	...	...	5
HD377	Field	39.6	G2	0.2	6250	1.00	1.50	1.0	...	...	5, 7
HD17925	Field	10	K1	0.0	5080	0.92	0.55	0.9	...	...	5, 7
HD32297	Field	112	A0	0.2	8000	1.90	6.20	1.3	...	...	5, 7
HD61005	Field	34	G8	0.1	5759	0.90	0.60	0.8	...	...	5, 7
HD69830	Field	13	G8	0.0	5500	0.90	0.60	0.85	...	...	5, 7
HD134319	Field	44	G5	0.0	5770	1.00	0.72	0.8	...	...	5, 7
HD216803	Field	8	K4	0.0	4600	0.66	0.19	0.7	...	...	5, 7
AOMen	Field	39	K3	0.0	4435	0.70	0.26	0.9	...	...	5

Notes. Objects marked with * are water-contaminated. ^{a}=Spectroscopic Binary treated as single star (22). Stars marked with ^{m} are binary or multiple systems with the following separation: AS 353A 5.″6 (22), CHX 22 0.″25 (24), DD Tau 0.″56 (49), DK Tau 2.″4 (22), DoAr 24E 2.″05 (39), DP Tau 0.″11 (22), HD 12039 0.″15 (2)—(this multiplicity has not been confirmed (12)), HD 142361 0.″73 (32)—(this multiplicity has not been confirmed (32, 25)), HK Tau 2.″4 (27), HN Tau 3.″1 (27), HT Lup 2.″8 (54), LkCa15 0.″08 (23), RX J1111.7-7620 0.″27 (24), RX J1612.6-1859 0.″21 (32), 1RXS J161411.0-230536 0.″22 (32), RW Aur 1.″4 (22), SR21 6.″4 (41), St 34 1.″18 (52), SX Cha 2.″2 (24), SZ Cha 5.″12 (24), UX TauA 2.7,0.″14 (10), UY Aur 0.″89 (27), V343NOR 10″ (45), VW Cha 0.64,0.″10 (24), WX Cha 0.″79 (24).

References. (1) Appenzeller et al. 1983; (2) Biller et al. 2007; (3) Brown et al. 2009; (4) Calvet et al. 2002; (5) Carpenter & Stauffer 2003 (6) Casali & Eiroa 1996 (7) Chen et al. 2014 (8) Cieza et al. 2010; (9) Cohen & Kuhi 1979; (10) Duchene et al. 1999; (11) Espaillat et al. 2012; (12) Evans et al. 2012; (13) Fernandez et al. 1995; (14) Furlan et al. 2006; (15) Furlan et al. 2011; (16) Guenther & Emerson 1997; (17) Herbig & Bell 1988; (18) Herbst 2008; (19) Hillenbrand et al. 2008; (20) Hughes & Hartigan 1992 (21) Kenyon et al. 1998; (22) Kraus et al. 2011; (23) Kraus & Ireland 2012; (24) Lafrenière et al. 2008; (25) Lafrenière et al. 2014; (26) Lahuis et al. 2007; (27) Leinert et al. 1993; (28) Levreault 1988; (29) Mamajek et al. 2004; (30) Manoj et al. 2011 (31) Merin et al. 2010; (32) Metchev & Hillenbrand 2009; (33) Muzerolle et al. 2010; (34) Nguyen et al. 2012; (35) Petrov et al. 2014 (36) Pinte et al. 2008; (37) Pontoppidan & Dullemond 2005; (38) Prato et al. 2003; (39) Ratzka et al. 2005; (40) Rebull et al. 2010; (41) Reipurth & Zinnecker 1993 (42) Reipurth et al. 1996; (43) Silverstone et al. 2006; (44) Strom et al. 1989 (45) Torres et al. 2008; (46) Uchida et al. 2004 (47) Walter 1986; (48) Walter 1992; (49) White & Ghez 2001; (50) White & Hillenbrand 2005; (51) White et al. 2007; (52) R. White et al., in preparation; (53) Wilking et al. 2005; (54) Woitas et al. 2001 (55) Zuckerman & Song 2004.

Table 6
Mid-IR Line Fluxes, Errors and Continuum Level around the Lines

Name	[Ne II]			H I (7–6)			H I (9–7)		
	Flux[a]	1σ[a]	Cont[b]	Flux[a]	1σ[a]	Cont[b]	Flux[a]	1σ[a]	Cont[b]
				Full disks					
IC348-2	7.66E-15	1.81E-15	0.24	4.05E-15	7.45E-16	0.25	<6.46E-15	...	0.33
IC348-6	<2.23E-15	...	0.078	<2.73E-15	...	0.077	<1.18E-14	...	0.11
IC348-31	<2.68E-15	...	0.076	<3.43E-15	...	0.067	<3.62E-15	...	0.067
IC348-37	<2.46E-15	...	0.055	<2.22E-15	...	0.059	<2.92E-15	...	0.081
IC348-55	2.16E-15	7.28E-16	0.034	<1.94E-15	...	0.037	<3.31E-15	...	0.052
IC348-68	<1.41E-15	...	0.011	2.68E-15	4.97E-16	0.011	<3.51E-15	...	0.012
04216+2603	<3.41E-15	...	0.20	<4.77E-15	...	0.20	<7.17E-15	...	0.23
04385+2550*	4.33E-15	1.66E-15	0.35	<7.61E-15	...	0.34	<1.08E-14	...	0.38
AA Tau*	1.32E-14	2.14E-15	0.31	<7.61E-15	...	0.32	<1.63E-14	...	0.41
BP Tau*	<5.61E-15	...	0.36	<6.70E-15	...	0.38	<1.80E-14	...	0.51
CW Tau*	<1.71E-14	...	1.13	3.45E-14 (5.73E-14)	4.20E-15	1.18	<3.73E-14	...	1.33
CX Tau	<2.38E-15	...	0.17	<3.01E-15	...	0.17	<5.55E-15	...	0.20
CY Tau*	2.22E-15	9.68E-16	0.15	<4.93E-15	...	0.16	<3.53E-15	...	0.18
DD Tau*	2.02E-14	4.73E-15	0.93	<1.37E-14	...	0.96	<5.02E-14	...	1.14
DE Tau	<5.75E-15	...	0.35	7.81E-15	1.40E-15	0.35	<1.34E-14	...	0.49
DG Tau	2.43E-13	1.13E-14	4.64	4.49E-14	6.49E-15	4.47	<5.44E-14	...	4.52
DK Tau*	<9.78E-15	...	0.78	<2.46E-14	...	0.88	<1.54E-14	...	1.24
DH Tau*	<3.99E-15	...	0.12	<4.01E-15	...	0.12	<1.04E-14	...	0.16
DL Tau*	1.24E-14	2.15E-15	0.87	7.12E-15 (3.24E-14)	2.09E-15	0.88	1.58E-14 (1.84E-14)	2.52E-15	0.93
DN Tau*	3.83E-15	5.38E-16	0.28	<3.22E-15	...	0.29	<2.92E-15	...	0.31
DO Tau*	<1.51E-14	...	1.89	<1.75E-14	...	1.94	<1.76E-14	...	2.17
DP Tau*	1.16E-13	3.63E-15	0.63	<2.42E-14	...	0.66	<2.44E-14	...	0.78
DQ Tau*	9.06E-15	3.33E-15	0.60	<1.14E-14	...	0.61	<1.19E-14	...	0.64
DR Tau*	<2.12E-14	...	1.88	3.46E-14 (1.03E-13)	6.93E-15	1.88	1.69E-14 (4.08E-14)	8.65E-15	2.10
DS Tau*	<6.33E-15	...	0.24	4.23E-15 (1.28E-14)	1.10E-15	0.25	<6.32E-15	...	0.36
FM Tau*	<2.26E-15	...	0.25	<4.85E-15	...	0.27	<6.71E-15	...	0.34
FN Tau	5.44E-15	1.23E-15	0.68	<5.71E-15	...	0.67	<5.59E-15	...	0.83
FT Tau*	5.97E-15	1.45E-15	0.25	<4.54E-15	...	0.26	<1.07E-14	...	0.31
FZ Tau*	<1.75E-14	...	0.98	2.46E-14 (8.65E-14)	3.42E-15	1.02	2.23E-14 (3.17E-14)	7.12E-15	1.15
HK Tau	5.51E-15	1.08E-15	0.20	3.44E-15	7.21E-16	0.20	<4.42E-15	...	0.24
HN Tau*	2.59E-14	4.81E-15	0.95	<1.66E-14	...	1.01	<4.05E-14	...	1.36
IP Tau	<6.22E-16	...	0.013	<8.16E-16	...	0.014	<1.94E-15	...	0.020
RW Aur*	<2.00E-14	...	1.43	1.96E-14 (7.16E-14)	5.92E-15	1.46	<3.23E-14	...	1.76
SU Aur	1.78E-14	3.63E-15	2.14	3.27E-14	3.87E-15	2.17	<7.15E-14	...	3.02
UYAur	<2.49E-14	...	2.36	<3.39E-14	...	2.38	<8.22E-14	...	2.67
AS 353A	1.11E-14	2.50E-15	1.11	1.96E-14	3.07E-15	1.13	<1.80E-14	...	1.26
LkHa326	4.74E-15	1.23E-15	0.33	<8.34E-15	...	0.33	<1.27E-14	...	0.36
2071-H13/ NGC 2068	1.01E-15	2.43E-16	0.024	<9.83E-16	...	0.026	<1.71E-15	...	0.038
NGC 20682071-S1	<1.97E-15	...	0.046	<1.77E-15	...	0.050	<2.23E-15	...	0.061
RX J1111.7-7620	9.97E-15	1.28E-15	0.22	<5.96E-15	...	0.23	<9.55E-15	...	0.27
SX Cha*	<7.08E-15	...	0.49	<1.34E-14	...	0.51	<1.42E-14	...	0.65
SZ50	<3.20E-15	...	0.20	<4.78E-15	...	0.21	<7.16E-15	...	0.22
TWCha	<4.35E-15	...	0.062	<4.01E-15	...	0.055	<6.63E-15	...	0.042
VW Cha*	3.13E-14	3.50E-15	0.73	3.74E-14 (5.98E-14)	2.79E-15	0.76	1.91E-14 (2.64E-14)	5.18E-15	0.95
VZ Cha*	<5.92E-15	...	0.37	<8.84E-15	...	0.40	<8.61E-15	...	0.46
WX Cha*	<5.08E-15	...	0.28	1.29E-14 (2.62E-14)	1.34E-15	0.30	<1.01E-14	...	0.43
XX Cha*	4.57E-15	7.48E-16	0.13	<5.66E-15	...	0.14	<6.46E-15	...	0.16
Hen-3-600A	<6.62E-15	...	0.099	<4.78E-15	...	0.095	<1.08E-14	...	0.11
TWA10	<2.44E-15	...	0.018	<2.09E-15	...	0.019	<3.05E-15	...	0.022
RX 132207.2-693812	<2.59E-14	...	0.75	3.46E-14	6.13E-15	0.74	3.17E-14	1.23E-14	0.84
EX Lup*	<1.63E-14	...	3.13	1.71E-14 (5.34E-14)	6.85E-15	3.21	<4.43E-14	...	4.12
GQ Lup*	<6.38E-15	...	0.49	4.39E-15 (1.23E-14)	2.29E-15	0.52	<9.91E-15	...	0.65
HTLup	<1.90E-14	...	2.17	<1.96E-14	...	2.21	<5.23E-14	...	2.64
RU Lup*	4.54E-14	8.41E-15	4.29	3.61E-14 (7.74E-14)	8.24E-15	4.36	<6.13E-14	...	4.80
RX J161411.0-230536	6.44E-15	1.36E-15	0.34	<5.69E-15	...	0.35	<7.30E-15	...	0.36
HD143006	<1.08E-14	...	0.69	<1.63E-14	...	0.74	<3.68E-14	...	1.12
DoAr 24E*	1.38E-14	4.20E-15	2.54	1.83E-14 (3.96E-14)	7.58E-15	2.58	<4.14E-14	...	2.96
DoAr 25*	2.87E-15	9.27E-16	0.21	<7.78E-15	...	0.22	<3.84E-15	...	0.24
SR21	<2.84E-14	...	0.79	<3.63E-14	...	0.75	<6.01E-14	...	0.91
Wa Oph6*	8.55E-15	1.83E-15	0.82	<2.25E-14	...	0.82	<1.65E-14	...	0.92
Ced110IRS2	<4.43E-15	...	0.11	1.92E-15	6.24E-16	0.12	<6.97E-15	...	0.15
Ced110-IRS4	2.43E-14	8.57E-16	0.080	<1.84E-15	...	0.070	<1.75E-15	...	0.054

Table 6
(Continued)

Name	[Ne II]			H I (7–6)			H I (9–7)		
	Flux[a]	1σ[a]	Cont[b]	Flux[a]	1σ[a]	Cont[b]	Flux[a]	1σ[a]	Cont[b]
Full disks									
Haro 1-16*	<9.73E-15	. . .	0.50	1.05E-14 (2.16E-14)	3.42E-15	0.54	<2.43E-14	. . .	1.05
RNO 90*	2.10E-14	1.08E-14	2.05	5.64E-14 (1.28E-13)	6.22E-15	2.10	3.87E-14 (4.92E-14)	9.83E-15	2.49
EC 82	1.39E-14	3.05E-15	1.32	<1.48E-14	. . .	1.45	<3.93E-14	. . .	2.57
RX J1842.9-3532	4.75E-15	7.21E-16	0.092	3.83E-15	7.96E-16	0.10	<5.25E-15	. . .	0.19
RX J1852.3-3700	8.66E-15	4.28E-16	0.035	4.62E-15	3.26E-16	0.037	<1.74E-15	. . .	0.055
V1331Cyg	<3.30E-15	. . .	1.01	1.16E-14	6.24E-16	0.96	<5.64E-15	. . .	0.95
Transitional disks									
IC348-21	3.12E-15	5.13E-16	0.088	3.71E-15	9.77E-16	0.081	<5.67E-15	. . .	0.11
IC348-67	2.40E-15	6.69E-16	0.018	<2.73E-15	. . .	0.019	<3.43E-15	. . .	0.023
IC348-72	<2.93E-15	. . .	0.011	<2.04E-15	. . .	0.011	<2.12E-15	. . .	0.012
IC348-133	<2.90E-15	. . .	0.017	<2.69E-15	. . .	0.016	<4.85E-15	. . .	0.023
DM Tau	5.45E-15	4.59E-16	0.047	<2.13E-15	. . .	0.048	<1.56E-15	. . .	0.055
FP Tau	<4.73E-15	. . .	0.067	<3.76E-15	. . .	0.070	<4.31E-15	. . .	0.078
GM Aur	1.02E-14	7.11E-16	0.097	1.89E-14	9.28E-16	0.10	1.20E-14	1.02E-15	0.17
LkCa 15	3.41E-15	5.54E-16	0.14	2.94E-15	6.71E-16	0.15	<7.89E-15	. . .	0.27
St 34	1.40E-15	5.66E-16	0.029	1.59E-15	4.68E-16	0.028	<2.12E-15	. . .	0.029
UX TauA	9.04E-15	9.85E-16	0.11	9.02E-15	8.53E-16	0.11	<4.98E-15	. . .	0.14
V836Tau	<2.05E-15	. . .	0.10	<3.61E-15	. . .	0.11	<3.33E-15	. . .	0.17
LkHa 330	<4.99E-15	. . .	0.49	8.84E-15	1.91E-15	0.50	<2.49E-14	. . .	0.69
2071-H9/ NGC 2068	1.21E-15	3.75E-16	0.023	2.44E-15	3.84E-16	0.024	<2.06E-15	. . .	0.038
CHX 22 (T54)	5.48E-15	9.30E-16	0.032	<2.57E-15	. . .	0.036	<1.04E-15	. . .	0.049
CS Cha	3.61E-14	6.12E-16	0.046	6.11E-15	2.53E-16	0.048	3.07E-15	7.43E-16	0.064
SZ Cha	1.48E-14	1.02E-15	0.16	6.10E-15	1.32E-15	0.17	<6.93E-15	. . .	0.25
SZ 18	7.63E-16	2.33E-16	0.0075	8.68E-16	2.14E-16	0.0073	<2.63E-15	. . .	0.0080
Sz 27 (T35)	6.32E-15	9.03E-16	0.021	3.03E-15	7.27E-16	0.022	<2.67E-15	. . .	0.026
TW Hya	5.01E-14	2.07E-15	0.61	7.93E-14	2.00E-15	0.62	3.34E-14	3.64E-15	0.81
IM Lup	7.03E-15	1.54E-15	0.48	<4.58E-15	. . .	0.49	<6.37E-15	. . .	0.60
DoAr 21	7.80E-14	2.58E-15	0.65	<1.32E-14	. . .	0.63	<4.66E-14	. . .	0.86
Debris disks									
1RXS J121236.4-55203	<6.09E-16	. . .	0.014	<8.71E-16	. . .	0.016	<8.11E-16	. . .	0.019
1RXS J122233.4-533347	<4.75E-16	. . .	0.020	8.56E-16	1.95E-16	0.021	<7.81E-16	. . .	0.026
1RXS J130153.7-53044	<4.95E-16	. . .	0.0084	<4.67E-16	. . .	0.0092	<8.19E-16	. . .	0.011
HD119269	<1.15E-15	. . .	0.024	<9.33E-16	. . .	0.026	<1.49E-15	. . .	0.031
1RXS J133758.0-413448	<6.79E-16	. . .	0.019	5.44E-16	2.04E-16	0.021	<8.21E-16	. . .	0.025
1RXS J161458.4-27501	<8.43E-16	. . .	0.0088	<6.31E-16	. . .	0.0098	<8.00E-16	. . .	0.012
HD 142361	<1.59E-15	. . .	0.040	2.98E-15	1.47E-16	0.043	1.44E-15	2.60E-16	0.052
RX 1600.0-2159	<7.96E-16	. . .	0.012	1.20E-15	1.91E-16	0.013	<7.63E-16	. . .	0.015
RX 1612.2-1859	<6.28E-16	. . .	0.028	9.32E-16	1.53E-16	0.031	<8.60E-16	. . .	0.036
HD 35850	3.38E-15	1.01E-15	0.26	9.02E-15	9.27E-16	0.27	<6.30E-15	. . .	0.34
V343Nor	<3.30E-15	. . .	0.11	4.81E-15	8.09E-16	0.12	<5.64E-15	. . .	0.15
HD19668	<1.14E-15	. . .	0.051	<1.62E-15	. . .	0.056	<2.56E-15	. . .	0.067
HD25457	<1.86E-14	. . .	0.53	<1.53E-14	. . .	0.58	<1.86E-14	. . .	0.68
HD37484	<2.66E-15	. . .	0.080	<2.16E-15	. . .	0.086	<4.47E-15	. . .	0.10
HD12039	<7.55E-16	. . .	0.065	<1.31E-15	. . .	0.071	<1.43E-15	. . .	0.082
HD202917	<1.94E-15	. . .	0.044	<3.19E-15	. . .	0.048	<4.31E-15	. . .	0.058
HD 141943	<1.27E-15	. . .	0.074	3.10E-15	4.13E-16	0.080	2.97E-15	4.91E-16	0.094
HD377	<1.79E-15	. . .	0.088	<1.31E-15	. . .	0.095	<2.73E-15	. . .	0.11
HD17925	<3.42E-15	. . .	0.61	<7.36E-15	. . .	0.66	<8.26E-15	. . .	0.78
HD32297	<3.26E-15	. . .	0.054	<4.28E-15	. . .	0.053	<5.09E-15	. . .	0.052
HD61005	<1.49E-15	. . .	0.066	<1.32E-15	. . .	0.072	<2.40E-15	. . .	0.084
HD69830	<4.54E-15	. . .	0.56	<4.75E-15	. . .	0.62	<1.05E-14	. . .	0.81
HD134319	<2.21E-15	. . .	0.047	<2.55E-15	. . .	0.051	<2.73E-15	. . .	0.060
HD216803	<5.66E-15	. . .	0.74	<7.99E-15	. . .	0.81	<6.96E-15	. . .	0.95
AOMen	<1.04E-15	. . .	0.051	<1.03E-15	. . .	0.056	<2.08E-15	. . .	0.065

Notes.

[a] Fluxes and errors are in erg s^{-1} cm^{-2}. For the detections we report the 1σ error, upper limits are at 3σ.

[b] Continua are in Jy. Objects marked with an * refer to water-contaminated disks, and the fluxes reported are already corrected for the water contribution. In parentheses we report the observed H I fluxes before the water subtraction.
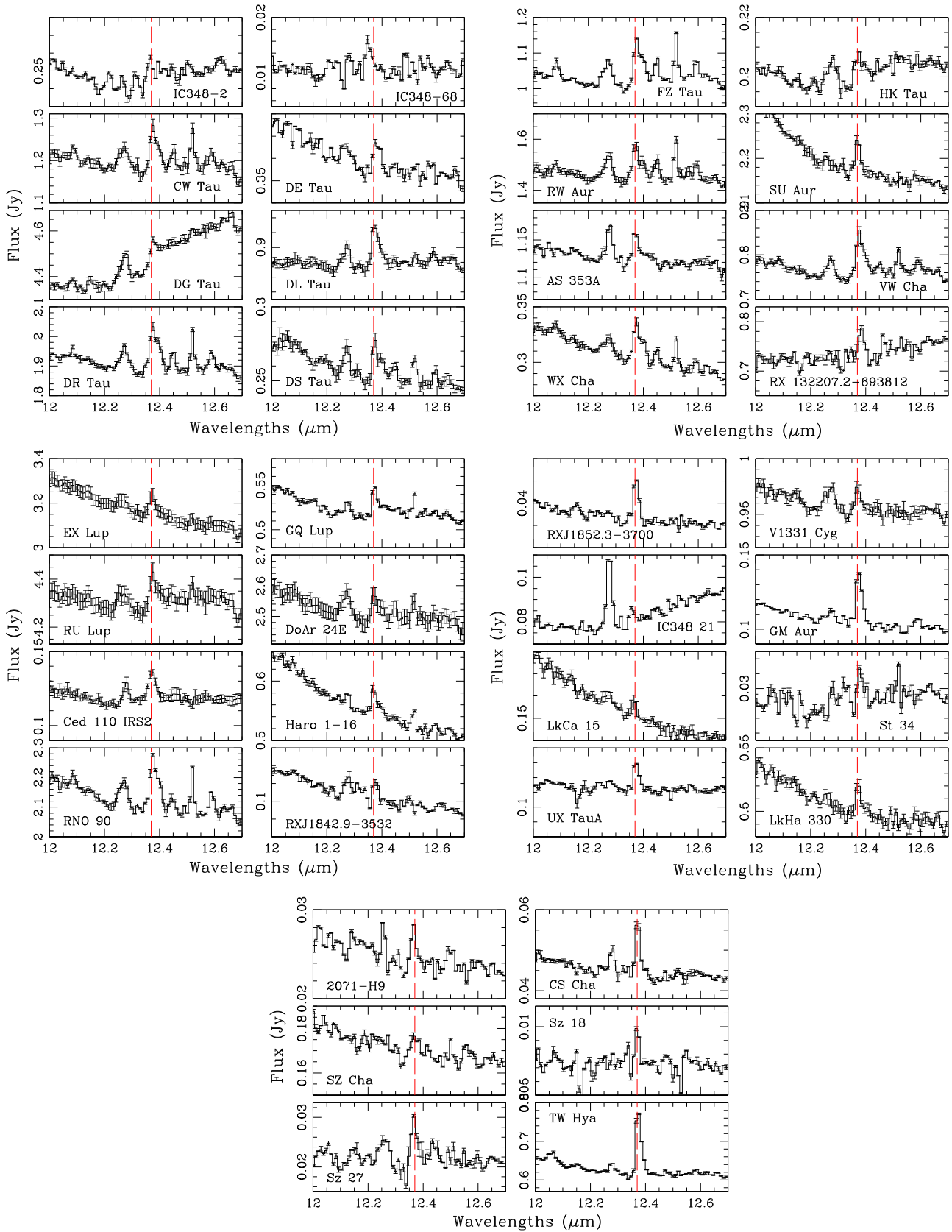
Figure 16. IRS spectra around the H I (7–6) line for the objects where the line is detected

less evolved, still embedded Class I objects (where the star is still surrounded by a remnant infall envelope and accretion disk). Still, care should be taken in converting the mid-IR H I line luminosities into mass accretion rate, because the envelope surrounding Class I sources could absorb part of the emission. More interestingly and on a speculative base, if the mid-IR H I lines were confirmed as accretion indicators in debris disks, these lines may be used to extend mass accretion rate

measurements to very low values. If the detected H I lines are indeed tracing accretion, the luminosities we measure for the eight debris disks correspond to mass accretion rates $\lesssim 10^{-10} M_\odot$ yr^{-1}. Optical and UV accretion diagnostics are not sensitive to such low mass accretion rates for Sun-like stars (e.g., Manara et al. 2013). Finally, extending accretion indicators to the mid-IR will enable simultaneous observations of the [Ne II] line (the only confirmed photoevaporative wind indicator) and the H I line (an accretion indicator), making possible a direct comparison of the two most efficient disk dispersal mechanisms, photoevaporation and viscous accretion (Alexander et al. 2014).

APPENDIX

In Figure 16 we show the H I (7–6) line for all the full and transitional disks where the line is detected. The H I (7–6) line profile for debris disks are shown in Figure 14. In Table 5 we report the source properties, and Table 6 report the mid-IR line fluxes, errors and continuum levels around the three line of interest.

REFERENCES

Alcalà, J. M., Natta, A., Manara, C., et al. 2014, A&A, 561, 2A
Alexander, R., Pascucci, I., Andrews, S., et al. 2014, in Protostars and Planets VI, ed., H. Beuther et al. (Tucson, AZ: Univ. Arizona Press), in press (arXiv:1311.1819)
Appenzeller, I., Krautter, J., & Jankovics, I. 1983, A&AS, 53, 291A
Baker, J. G., & Menzel, D. H. 1938, ApJ, 88, 52B
Baldovin-Saavedra, C., Audard, M., Carmona, A., et al. 2012, A&A, 543A, 30B
Baldovin-Saavedra, C., Audard, M., Güdel, M., et al. 2011, A&A, 528A, 22B
Baliunas, S., Sokoloff, D., & Soon, W. 1996, ApJL, 457, L99
Banzatti, A., Meyer, M., Pontoppidan, K., & Bruderer, S. 2013, prpl.conf2S034B
Bary, J. S., Matt, S. P., Skrutskie, M. F., et al. 2008, ApJ, 687, 376B
Basri, G., & Batalha, C. 1990, ApJ, 363, 654B
Biller, B., Close, L., Masciadri, E., et al. 2007, ApJS, 173, 143B
Brown, J. M., Blake, G. A., Qi, C., et al. 2009, ApJ, 704, 496
Calvet, N., D'Alessio, P., Hartmann, L., et al. 2002, ApJ, 568, 1008
Calvet, N., & Hartmann, L. 1992, ApJ, 386, 239C
Calvet, N., Muzerolle, J., Briceño, C., et al. 2004, AJ, 128, 1294C
Carpenter, J., & Stauffer 2003, FEPS Memo, No. 4, http://feps.as.arizona.edu/index.html
Carr, J., & Najita, J. 2008, Sci, 319, 1504C
Carr, J., & Najita, J. 2011, ApJ, 733, 102
Casali, M. M., & Eiroa, C. 1996, A&A, 306, 427C
Chen, C. H., Mittal, T., Kuchner, M., et al. 2014, ApJS, 211, 25
Cieza, L., Schreiber, M., Romero, G., et al. 2010, ApJ, 712, 925
Cohen, M., & Kuhi, L. V. 1979, ApJS, 41, 743C
Costigan, G., Scholz, A., Stelzer, B., et al. 2012, MNRAS, 427, 1344C
Dent, W. R. F., Thi, W. F., Kamp, I., et al. 2013, PASP, 125, 477D
Duchene, G., Monin, J., Bouvier, J., & Menard, F. 1999, A&A, 351, 954D
Dutrey, A., Semenov, D., Chapillon, E., et al. 2014, in Protostars and Planets VI, ed., H. Beuther et al. (Tucson, AZ: Univ. Arizona Press), in press (arXiv:1402.3503)
Edwards, S., Kwan, J., Fischer, W., et al. 2013, ApJ, 778, 148E
Ercolano, B., Drake, J. J., Raymond, J. C., & Clarke, C. C. 2008, ApJ, 688, 398E
Ercolano, B., & Owen, J. 2010, MNRAS, 406, 1553
Espaillat, C., Ingleby, L., Furlan, E., et al. 2013, ApJ, 762, 62E
Espaillat, C., Ingleby, L., Hernàndez, J., et al. 2012, ApJ, 747, 103
Evans, T. M., Ireland, M. J., Kraus, A. L., et al. 2012, ApJ, 744, 120
Fang, M., van Boekel, R., Wang, W., et al. 2009, A&A, 504, 461F
Feigelson, E., Townsley, L., Güdel, M., & Stassun, K. 2007, in Protostars and Planets V, ed. B. Reipurth, D. Jewitt, & K. Keil (Tucson, AZ: Univ. Arizona Press), 313F
Fernandez, M., Ortiz, E., Eiroa, C., & Miranda, L. F. 1995, A&AS, 114, 439F
Folha, D. F. M., & Emerson, J. P. 2001, A&A, 365, 90F
Furlan, E., Hartmann, L., Calvet, N., et al. 2006, ApJS, 165, 568F
Furlan, E., Luhman, K., Espaillat, C., et al. 2011, ApJS, 195, 3
Giampapa, M. S., Calvet, N., Imhoff, C. L., & Kuhi, L. V. 1981, ApJ, 251, 113G
Gray, R. O., Corbally, C. J., Garrison, R. F., et al. 2006, AJ, 132, 161G
Güdel, M., Lahuis, F., Briggs, K. R., et al. 2010, A&A, 519A, 113G
Guenther, E. W., & Emerson, J. P. 1997, A&A, 321, 803G
Gullbring, E., Hartmann, L., Briceño, C., & Calvet, N. 1998, ApJ, 492, 323G
Hartigan, P., Edwards, S., & Ghandour, L. 1995, ApJ, 452, 736H
Hartmann, L., Avrett, E. H., Loeser, R., & Calvet, N. 1990, ApJ, 349, 168H
Henry, T. J., Soderblom, D. R., Donahue, R. A., & Baliunas, S. L. 1996, AJ, 111, 439
Herbig, G. H., & Bell, K. 1988, LicOB, 1111, 90
Herbst, W. 2008, Handbook of Star Forming Regions, Vol. II (San Francisco, CA: ASP)
Herczeg, G., Najita, J., Hillenbrand, L., & Pascucci, I. 2007, ApJ, 670, 509H
Higdon, S. J. U., Devost, D., Higdon, J. L., et al. 2004, PASP, 116, 975
Hillenbrand, L., Carpenter, J., Kim, S. J., et al. 2008, ApJ, 677, 630
Hollenbach, D., & Gorti, U. 2009, ApJ, 703, 1203
Houck, J., Roellig, T. L., van Cleve, J., et al. 2004, ApJS, 154, 18H
Hughes, J., & Hartigan, P. 1992, AJ, 104, 680H
Hummer, D. G., & Storey, P. J. 1987, MNRAS, 224, 801H
Ingleby, L., Calvet, N., Herczeg, G., et al. 2013, ApJ, 767, 112I
Johns-Krull, C. 2007, ApJ, 664, 975J
Keane, J. T., Pascucci, I., Espaillat, C., et al. 2014, ApJ, 787, 153K
Kelly, B. C. 2007, ApJ, 665, 1489K
Kenyon, S. J., Brown, D., Tout, C., & Berlind, P. 1998, AJ, 115, 2491
Kenyon, S. J., & Hartmann, L. 1995, ApJS, 101, 117K
Kraus, A., & Ireland, M. 2012, ApJ, 745, 5K
Kraus, A., Ireland, M., Martinache, F., & Hillenbrand, L. 2011, ApJ, 731, 8K
Kwan, J., & Fischer, W. 2011, MNRAS, 411, 2383K
Lafrenière, D., Jayawardhana, R., Brandeker, A., et al. 2008, ApJL, 683, L844
Lafrenière, D., Jayawardhana, R., van Kerkwijk, M. H., et al. 2014, ApJL, 785, L47
Lahuis, F., van Dishoeck, E., Blake, G., et al. 2007, ApJL, 665, L492
Leinert, C., Zinnecker, H., Weitzel, N., et al. 1993, A&A, 278, 129L
Levreault, R. 1988, ApJL, 330, L897
Luhman, K. L., Stauffer, J. R., & Mamajek, E. E. 2005, ApJL, 628, L69
Luhman, K. L., Stauffer, J. R., Muench, A. A., et al. 2003, ApJL, 593, L1093
Mamajek, E., Meyer, M., Hinz, P., et al. 2004, ApJ, 612, 496M
Mamajek, E., Meyer, M., & Liebert, 2002, AJ, 124, 1670
Manara, C. F., Testi, L., Natta, A., et al. 2014, A&A, 568A, 18M
Manara, C. F., Testi, L., Rigliaco, E., et al. 2013, A&A, 551, 107
Manoj, P., Kim, K. H., Furlan, E., et al. 2011, ApJS, 193, 11M
Martin, S. C. 1996, ApJ, 470, 537M
Mathis, J. S. 1990, in ASP Conf. Ser. 12, The Evolution of the Interstellar Medium, ed, L. Blitz (San Francisco, CA: ASP), 63M
McCabe, C., Ghez, A. M., Prato, L., et al. 2006, ApJ, 636, 932M
Meijerink, R., Pontoppidan, K. M., Blake, G. A., et al. 2009, ApJ, 704, 1471M
Merin, B., Brown, J., Oliveira, I., et al. 2010, ApJ, 718, 1200M
Metchev, S. A., & Hillenbrand, L. 2009, ApJS, 181, 62M
Meyer, M., Hillenbrand, L., Backman, D., et al. 2006, PASP, 118, 1690M
Muzerolle, J., Allen, L., Megeath, S., et al. 2010, ApJ, 708, 1107M
Muzerolle, J., Calvet, N., & Hartmann, L. 2001, ApJ, 550, 944M
Muzerolle, J., Hartmann, L., & Calvet, N. 1998, AJ, 116, 455M
Najita, J., Carr, J., Strom, S., et al. 2010, ApJ, 712, 274
Natta, A., Testi, L., & Randich, S. 2006, A&A, 452, 245N
Nguyen, D. C., Brandeker, A., van Kerkwijk, M. H., & Jayawardhana, R. 2012, ApJ, 745, 119
Noyes, R. W., Hartmann, L. W., Baliunas, S. L., et al. 1984, ApJ, 279, 763N
Pascucci, I., Gorti, U., Hollenbach, D., et al. 2006, ApJ, 651, 1177P
Pascucci, I., Herczeg, G., Carr, J. S., & Bruderer, S. 2013, ApJ, 779, 178P
Pascucci, I., Hollenbach, D., Najita, J., et al. 2007, ApJ, 663, 383
Pascucci, I., & Sterzik, M. 2009, ApJ, 702, 724P
Patten, B., & Simon, T. 1996, ApJS, 106, 489P
Petrov, P. P., Kurosawa, R., Romanova, M. M., et al. 2014, MNRAS, 442, 3643P
Pinte, C., Padgett, D., Ménard, F., et al. 2008, A&A, 489, 633
Pontoppidan, K., & Dullemond, K. 2005, A&A, 435, 595
Pontoppidan, K., Salyk, C., Bergin, E., et al. 2014, in Protostars and Planets VI, ed., H. Beuther et al. (Tucson, AZ: Univ. Arizona Press), in press (arXiv:1401.2423)
Pontoppidan, K., Salyk, C., Blake, G., & Káufl, H. 2010, ApJL, 722, L173
Prato, L., Greene, T. P., & Simon, M. 2003, ApJ, 584, 853P
Preibisch, T., Brown, A., Bridges, T., et al. 2002, AJ, 124, 404

Ratzka, T., Köhler, R., & Leinert, Ch. 2005, A&A, 437, 611
Ratzka, T., Leinert, C., Henning, T., et al. 2007, A&A, 471, 173R
Rebull, L. M., Padgett, D. L., McCabe, C., et al. 2010, ApJS, 186, 259R
Reipurth, B., Pedrosa, A., & Lago, M. 1996, A&AS, 120, 229R
Reipurth, B., & Zinnecker, H. 1993, A&A, 278, 81R
Rigliaco, E., Natta, A., Randich, S., & Sacco, G. 2009, A&A, 495L, 13R
Rigliaco, E., Natta, A., Testi, L., et al. 2012, A&A, 548A, 56R
Riviere-Marichalar, P., Ménard, F., Thi, W. F., et al. 2012, A&A, 538L, 3R
Rothman, L. S., Gordon, I. E., Barbe, A., et al. 2009, JQSRT, 110, 533R
Sacco, G. G., Flaccomio, E., Pascucci, I., et al. 2012, ApJ, 747, 142S
Salyk, C., Herczeg, G., Brown, J., et al. 2013, ApJ, 769, 21S
Salyk, C., Pontoppidan, K., Geoffrey, A., et al. 2008, ApJ, 676L, 49S
Salyk, C., Pontoppidan, K. M., Blake, G. A., et al. 2011, ApJ, 731, 130S
Siess, L., Dufour, E., & Forestini, M. 2000, A&A, 358, 593S
Silverstone, M. D., Meyer, M. R., Mamajek, E. E., et al. 2006, ApJ,
    639, 1138S
Storey, P. J., & Hummer, D. G. 1995, MNRAS, 272, 41S
Strom, K. M., Strom, S. E., & Margulis, M. 1989, ESOC, 33, 423S

Testi, L., Birnstiel, T., Ricci, L., et al. 2014, in Protostars and Planets VI, ed., H.
    Beuther et al. (Tucson, AZ: Univ. Arizona Press), in press (arXiv:1402.1354)
Torres, C. A. O., Quast, G. R., Melo, C. H. F., & Sterzik, M. F. 2008, in
    Handbook of Star Forming Regions, Volume II: The Southern Sky, ed. B.
    Reipurth (ASP Monograph Publications, Vol. 5; San Francisco, CA: ASP),
    757
Uchida, K. I., Calvet, N., Hartmann, L., et al. 2004, ApJS, 154, 439
van Boekel, R., Güdel, M., Henning, T., et al. 2009, A&A, 497, 137V
Walter, F. M. 1986, ApJ, 306, 573W
Walter, F. M. 1992, AJ, 104, 758
White, R., & Ghez, A. 2001, ApJ, 556, 265W
White, R. J., Gabor, J. M., & Hillenbrand, L. 2007, AJ, 133, 2524W
White, R. J., & Hillenbrand, L. 2005, ApJ, 621L, 65W
Wilking, B., Meyer, M., Robinson, J., & Greene, T. 2005, AJ, 130, 1733W
Woitas, J., Leinert, Ch., & Köhler, R. 2001, A&A, 376, 982W
Wright, J. T., Marcy, G. W., Butler, R. P., & Vogt, S. S. 2004, ApJS, 152, 261
Zuckerman, B., & Song, I. 2004, ARA&A, 42, 685Z
Zuckerman, B., Song, I., & Webb, R. A. 2001, ApJ, 559, 388